Supplementary Information

Understanding mechanical failure behaviours and protocol optimization for fast charging applications in Co-free Ni-based cathodes for lithium-ion batteries†

Jaesub Kwon[1‡], Jaehyun Kim[2‡], Jong-Heon Lim[3], Kyoung Eun Lee[3], Seok-Mun Kang[4], Youngsun Kong[4], Dong-Hyun Kim[5], Kyu-Su Kim[1], Gogwon Choe[1], Sang-Mun Jung[1], Docheon Ahn[6], Yoon-Uk Heo[5], Janghyuk Moon[2] *, Kyu-Young Park[1 3] * and Yong-Tae Kim[1 5]*

1. *Department of Materials Science and Engineering, Pohang University of Science and Technology (POSTECH), Pohang 37673, Republic of Korea*
2. *Department of Energy Systems Engineering, Chung-Ang University, 84 Heukseok-ro, Dongjak-gu, Seoul 06974, Republic of Korea*
3. *Department of Battery Engineering in GIFT, Pohang University of Science and Technology (POSTECH), Pohang 37673, Republic of Korea*
4. *SDI R&D Center, Samsung SDI Co., LTD, 130 Samsung-ro, Yeongtong-gu, Suwon-si, Gyeonggi-do, 16678, Republic of Korea*
5. *Graduate Institute of Ferrous and Eco Materials Technology, Pohang University of Science and Technology (POSTECH), Pohang, 37673, Republic of Korea*
6. *Beamline Division, PLS-II, Pohang Accelerator Laboratory (PAL), Pohang, 37673 Republic of Korea*

‡ These authors contributed equally to this work

* Corresponding e-mail:

jhmoon84@cau.ac.kr, kypark0922@postech.ac.kr, and yongtae@postech.ac.kr

1. Methods

1.1. Material synthesis

The Co-free LNMO hydroxide precursor sourced from Samsung SDI was utilized for this study. Each precursor was blended with anhydrous LiOH in accordance with a molar ratio of Li:(Ni+Mn) = 1.03:1 to mitigate the loss of lithium due to high temperature-induced evaporation. The resultant mixtures were subjected to calcination in a tube furnace under a flowing O_2 atmosphere. The calcination process involved a two-step heating procedure, with a ramping rate of 3 °C min^{-1}. Initially, the temperature was raised to 500 °C and held for 6 hours to facilitate the liquefaction of LiOH, followed by a second step where the target temperature was maintained for 8 hours to ensure complete synthesis of the layered structure. Subsequently, the powders were allowed to cool within the furnace.

1.2. Electrochemical characterization

For the electrochemical experiments, the LNMO cathode was combined with a conducting agent and a binder material. The cathode was prepared with a composition of LNMO:Super P:PVDF in a ratio of 8:1:1, with 12wt% PVDF (KF1120, KUREHA) dissolved in N-methyl-2-pyrrolidone (NMP) using a Thinky mixer (Thinky Mixer, ARM-310). The resulting slurry was coated onto Al foil (Hohsen) using a doctor blade (Hohsen), with an active material loading of 3 $mgcm^{-2}$. After drying in a vacuum oven, the coated foil was roll-pressed to achieve a density of 3 $mgcm^{-3}$. The electrolyte used was 1 M $LiPF_6$ in EC:DMC:EMC = 3:4:3 v/v (Hohsen). Half-cell electrochemical cells were assembled using 2032 coin-type cells (Hohsen Corporation, CR2032) with Li metal anode (MTI corporation, EQ-Lib-LiC25-1400) and GF/F (Cyvita, Whatman GF/F) separators. The cells were rested for 12 hours and then subjected to 2 cycles at 0.2C, with voltage limits of 3.0V – 4.3 V vs Li/Li^+ foil for precycles

(WonATech, WBCS3000L), where 1C=200mA/g. Galvanostatic intermittent titration technique (GITT) measurements were performed after one galvanostatic cycling at 0.1C to compare the Li ion diffusivity of LNMO. A current of 0.1C was applied for 10 minutes followed by a 30-minute rest period, over a voltage range of 3.0 V to 4.3 V. The Li ion diffusion coefficient (DLi) was calculated using the cathode's surface area determined via Brunauer-Emmett-Teller (BET) testing. The exchange current of LNMO was determined using electrochemical impedance spectroscopy (WonATech, ZIVE SP1) over a frequency range from 10^5 Hz to 10^{-2} Hz, after charging to the target state of charge (SOC).

1.3. Synchrotron based ex-situ and operando material characterization

To clearly demonstrate the bulk structure of the synthesized LNMO powder, we utilized hard X-ray and soft X-ray synchrotron-based analysis from Pohang Accelerators Laboratory (PAL). The lattice structure of the LNMO were examined from the 9B-high resolution powder diffraction (HRPD) beamline with a wavelength of 1.52150 Å. After that Rietveld refinement was performed via Fullprof Suite software. Hard X-ray absorption spectroscopy (XAS) was performed from 8C-Nanoprobe XAFS beamline from the PAL. The cathode powders were loaded on the holder in the Ar filled glove box to reduce the effect of air exposure to the samples. Spectra were plotted using ATHENA software package, while all spectra were aligned by reference foil. In-situ XRD analysis were conducted at 9A U-SAXS beamline, in wide angle x-ray scattering (WAXS) mode. The coin cell with kepton window were carefully placed in the X-ray beam source with the energy of 19.75 keV. The diffraction image were recorded during electrochemical cycling in the exposure time of 1 s to the 2 dimensional charge-coupled device (CCD) detector (SX165, Rayonix, USA).

1.4. Other characterization

Pre, and post-mortem microstructure analysis of cathode were conducted with SEM (HITACHI S-4800). For post-mortem characterization, cycled electrode were disassembled in Ar filled glove box and rinsed with anhydrous DMC solvent and dried at room temperature. Dried electrodes underwent polishing using cross-section polisher (Leica EM TIC 3X, Leica Ltd., Germany) with an accelerated voltage of 5kV for a duration of 6 hours to achieve a finely polished surface. Quenching X-ray diffraction (XRD) experiment were conducted after terminating experiment cells were disassembled in 2 min to terminate interparticle Li ion exchange and rinsed with anhydrous DMC solvent and dried at room temperature. Lab scale XRD measurements were performed by a D8 Advance X-ray diffractometer (Bruker, Germany) with Cu Kα radiation at a scan rate of 1°/min. The chemical compositions of the Co-free LNMO cathodes were ascertained via Inductively coupled plasma mass spectrometry (ICP-MS, PerkinElmer, NexION 300s). Co-free LNMO cathodes were dissolved in aqua regia (HCl:HNO3 = 3:1). Subsequently, all dissolved samples underwent dilution with deionized water to ensure that the concentration of the target element fell within the bounds of a calibration curve, thus ensuring high reliability in the measurements. The calibration curves were constructed employing a minimum of three (1, 5, 10 ppb) standard solutions, with results considered only if correlation coefficients exceeded 0.999 and the relative standard deviation (RSD) was below 5%.

1.5. Finite element analysis

The finite element analyses of coupled Li kinetics and solid mechanics of LNMO were conducted using the commercial software COMSOL Multiphysics V6.2. The diffusion of Li inside an electrode particle is described by Fick's second law of diffusion, which is a mass conservation equation given by[1]

$$\frac{\partial c}{\partial t} + \nabla \cdot J = 0$$

where c is the concentration of Li and J is the Li flux inside the electrode particle. J is defined using Fick's first law of diffusion, which is expressed as

$$J = -D\nabla c$$

where D is the Li diffusion coefficient inside the particle. Due to the layered structure of Ni-Mn binary oxide cathodes, Li diffusion across the layers is reduced to an order of 10 to hinder the effect of c-lattice diffusion[2].

A limitation of our simulation is that it is limited to a single particle model. Therefore, the applied current density i_n (1 C current = 0.448 A/m^2) should be converted into Li inward flux. The Li inward flux J is expressed as

$$J = \frac{i_n}{F}$$

where F represents the Faraday's constant (96,485 C/mol).

The compositional strain generated from the diffusion of Li inside the particle is expressed as[3]

$$\epsilon_{ij}^{c} = \Delta c \frac{\Omega}{3} \delta_{ij}$$

where ϵ_{ij}^{c} is the compositional strain tensor, Ω is the partial molar volume of Li and δ_{ij} is the Kronecker delta. The elastic strain tensor of an electrode particle is expressed as[4]

$$\epsilon_{ij}^{e} = S_{ijkl}\sigma_{kl}$$

where ϵ_{ij}^{e} is the elastic strain tensor, S_{ijkl} is the compliance tensor and σ_{kl} is the stress tensor. Therefore, the total strain tensor ϵ_{ij} generated within the electrode particle, which undergoes

compositional strain and elastic strain is expressed as[5]

$$\epsilon_{ij} = \epsilon_{ij}^{e} + \epsilon_{ij}^{c}$$

The Cohesive Zone Model (CZM) was employed to simulate the damage and brittle fracture across the grain boundaries of secondary particles in an electrode[6]. The damage of a particle begins to develop when the traction, which is proportional to the separation δ and penalty factor K reaches the tensile strength of the particle σ_t. When damage develops in the particle, the irreversible softening within the particle begins. The value of K decreases as damage accumulates, eventually reaching zero when fracture is initiated (**Figure S25**). The separation length δ_d at which damage starts to develop is expressed as

$$\delta_d = \frac{\sigma_t}{K}$$

The separation length where the fracture initiates δ_f is expressed as

$$\delta_f = \frac{2G_c}{\sigma_t}$$

where G_c is the critical energy release rate of the particle, which indicates the amount of energy required for fracture to be initiated. In our simulation, the damage has been assumed to be developed to 0.9 to model the fracture behavior after 100 cycles.

The 5C/CV charging process simulation is designed under equation below, as the current exponentially decays under potentiostatic charging process. Parameters are available in **Table S8**.

$$CCCV = 5i_0 e^{-\frac{c_{max}}{c_{average}}}$$

$$i_{CCCV} = if(t < 390, i_0, CCCV)$$

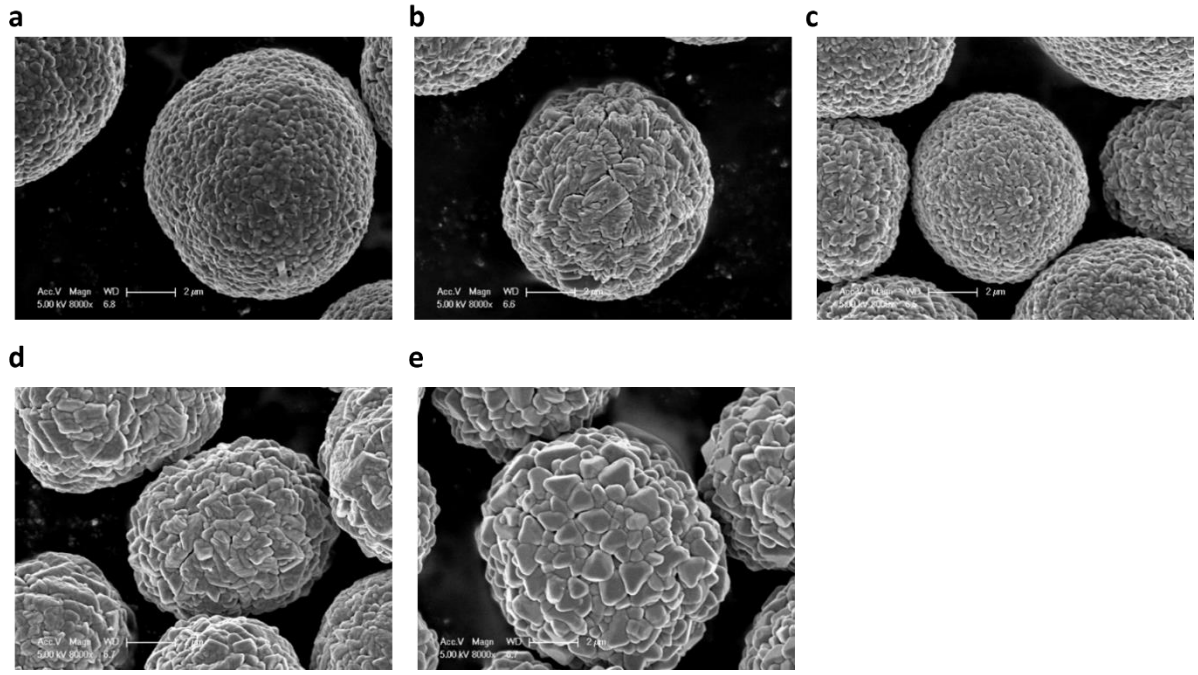

Figure S1. SEM images of synthesized **a)** LNO, **b)** NM90, **c)** NM80 **d)** NM70, and **e)** NM66

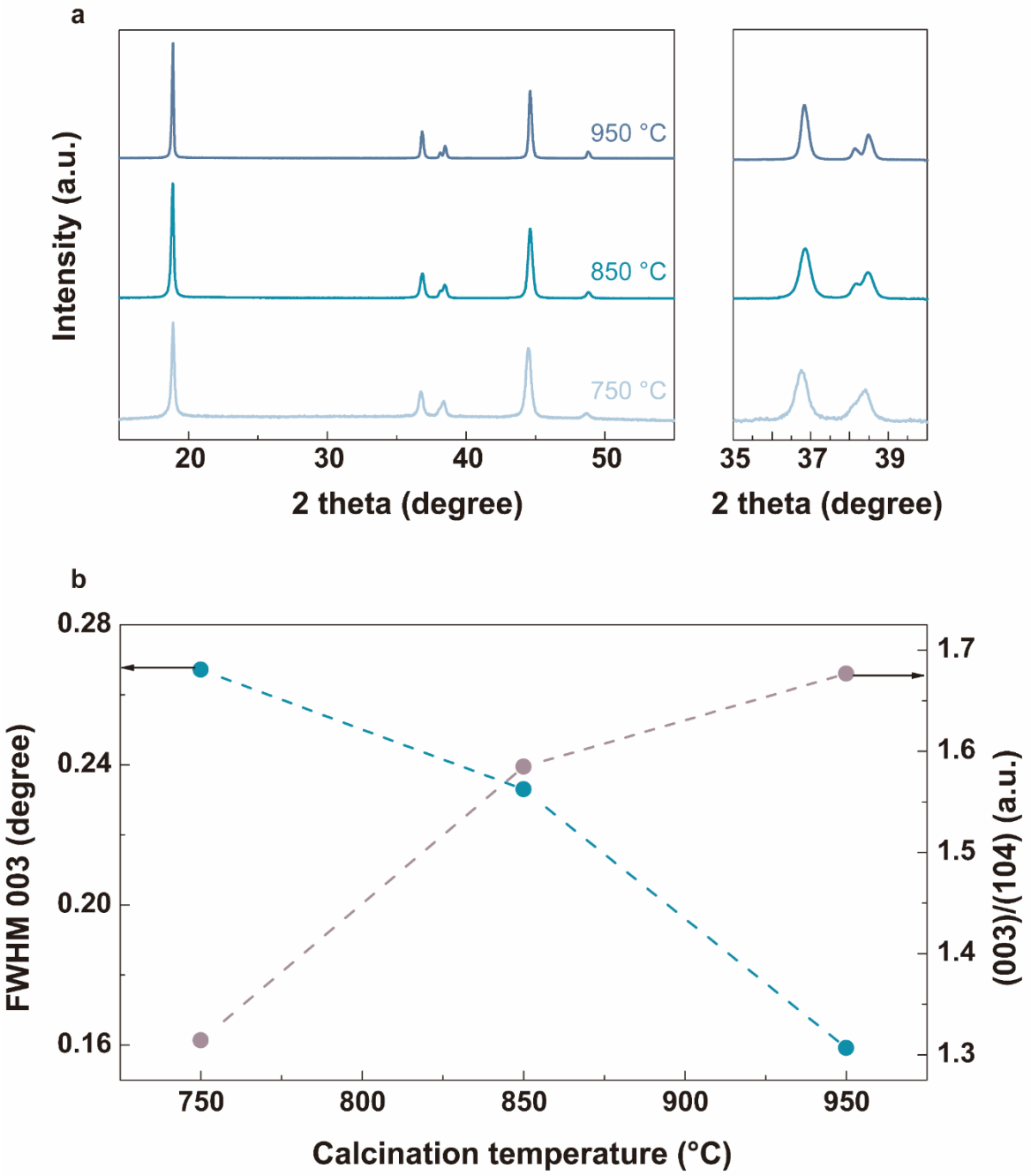

Figure S2. XRD analysis for calcination temperature effect on NM66 **a)** XRD profile of different calcination temperature **b)** FWHM of (003) peak to clarify crystallinity and (003)/(104) for Li/Ni disorder. Here the lower FWHM003 and higher (003)/(104) ratio each indicates higher crystallinity and lower Li/Ni disorder respectively

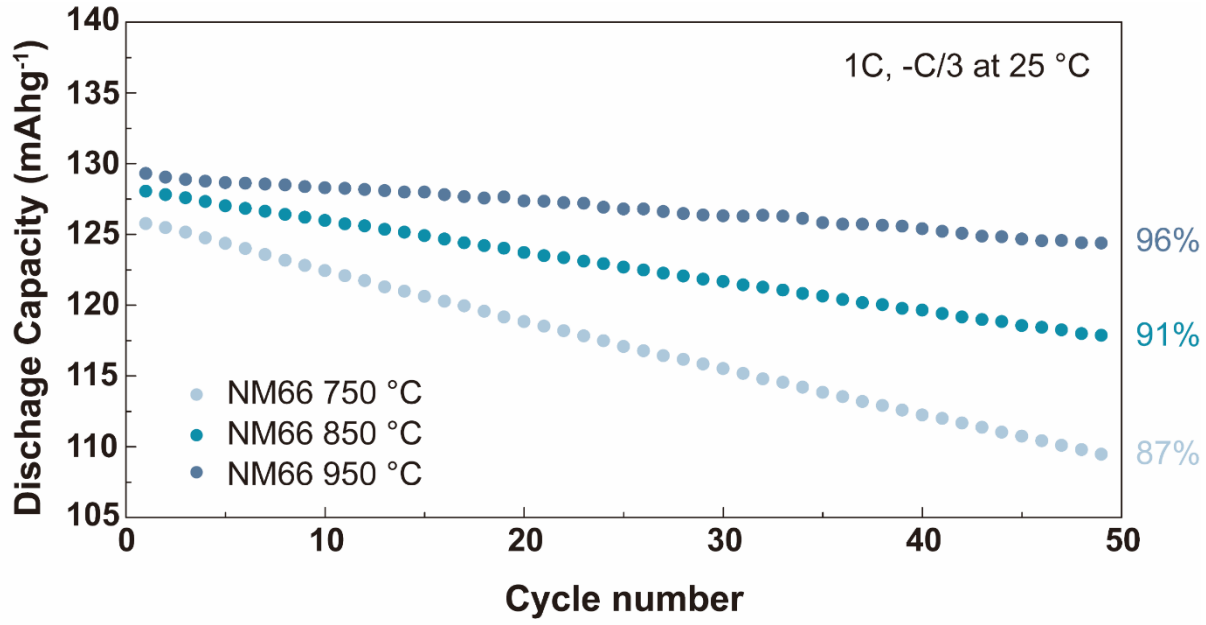

Figure S3. Cycle retention of different calcination temperature of NM66 for optimizing calcination temperature of NM66. The electrochemical cycling data rationalize the optimized synthesis temperature of NM66 is 950 ℃.

Supporting Table 1. Calcination temperature of Co-free LNMO

Sample	Precursor	Temperature
LNO	$Ni(OH)_2$	720 ℃
NM90	$Ni_{0.90}Mn_{0.10}(OH)_2$	740 ℃
NM80	$Ni_{0.80}Mn_{0.20}(OH)_2$	830 ℃
NM70	$Ni_{0.70}Mn_{0.30}(OH)_2$	880 ℃
NM66	$Ni_{0.66}Mn_{0.34}(OH)_2$	950 ℃

Supplementary Note 1

The calcination temperature of layered oxide cathodes plays a crucial role in determining their material properties. For instance, Li/Ni disorder typically rises with increasing calcination temperature due to the increased configurational entropy, which thermodynamically favors defect formation[7] . Additionally, higher calcination temperatures promote the crystal growth of primary particles because Ostwald ripening, the anticipated crystal growth mechanism in high-Ni cathodes during calcination, is enhanced by greater atomic mobility under these conditions[8]. Li/Ni disorder and crystallite size significantly controls the electrochemical property of cathode materials such as, energy density, rate capability and cyclability.

Accordingly, proper calcination of Co-free LNMO is determined with XRD analysis and subsequent electrochemical analysis as the NM66 with different calcination temperature is represented at **Figure S2** and **S3**. Universal crystallographic information of the calcined NM66 is analyzed via peak separation, full width at half maximum (FWHM) and peak intensity ratio[9]. Peak separation of (006) / (012) and higher value of (003) / (104) peak ratio corresponds to layered structure ordering, indicates that higher calcination temperature (950 ℃) is required to form proper layered structure in NM66. FWHM of (003) peak NM66 decreases as the calcination temperature increases indicating that crystallite size of primary particle increases at higher calcination temperature. Electrochemical test were conducted for NM66 different calcination temperature, and cyclability of 950 ℃ calcined NM66 was greatest among the different temperature calcined NM66 and the retention is comparable to previous studies with similar composition[10]. Based on similar XRD and electrochemical analysis we determined the proper calcination temperature for the series of Co-free LNMO cathodes.

Supporting Table 2. Chemical composition of Co-free LNMO

Chemical composition of Co-free $LiNi_xMn_{1-x}O_2$ cathode

Atomic fraction (%)	Ni	Mn
x=1.00	100	N/D
x=0.90	89.50	10.50
x=0.80	79.63	20.37
x=0.70	69.54	30.46
x=0.66	65.79	34.21

N/D : Not detected

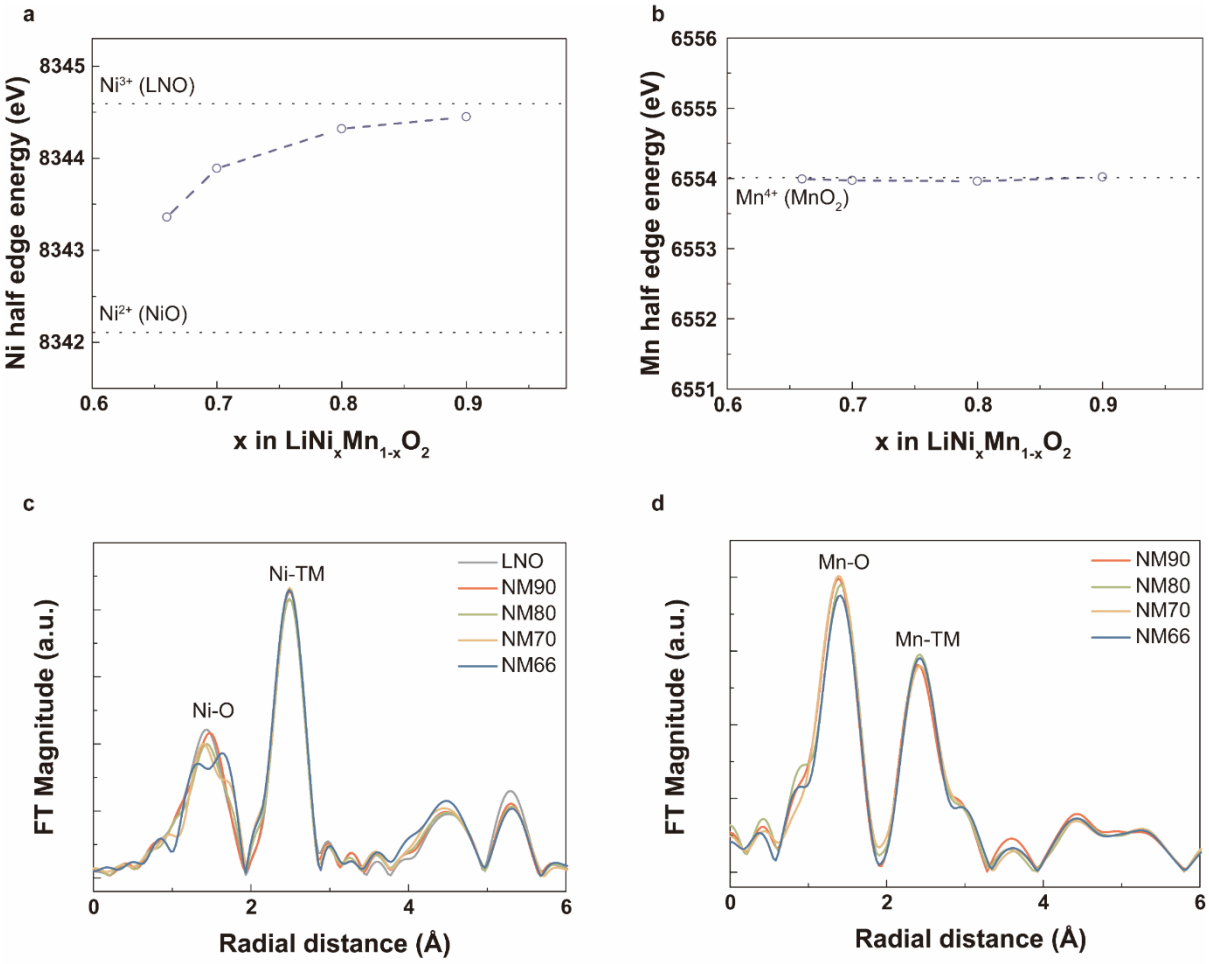

Figure S4. X-ray absorption spectroscopy

a) Half cut energy of Ni K-edge and **b)** Half cut energy of Mn K-edge from XANES spectra. Radial distribution function (RDF) of **c)** Ni and **d)** Mn.

The XANES spectra of Ni underwent redshift with Mn substitution and the Ni-O bond from RDF clearly shows that Ni oxidation states varies with Mn substitution. While the spectrum of Mn was relatively invariant. Moreover, the first shell in the Ni RDF, corresponds to 1st neighbor Ni-O bond, exhibited peak splitting with Mn substitution, further verifies the gradually Ni reduction with Mn^{4+} substitution.

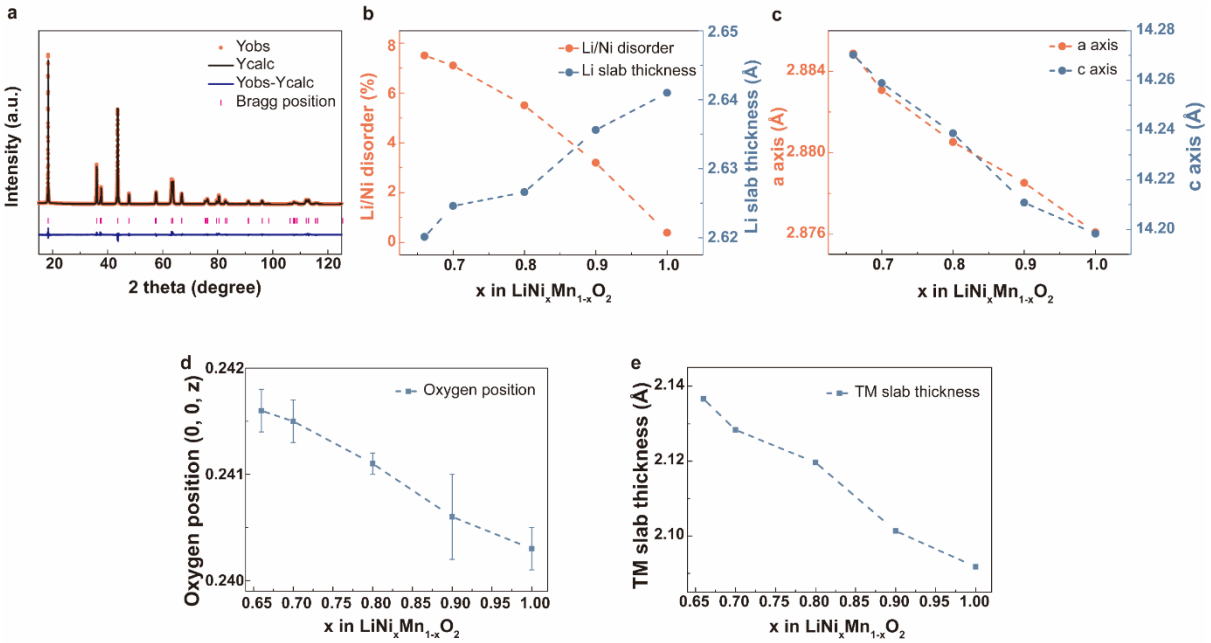

Figure S5. Rietveld refinement results of LNMO

a) Representative Rietveld refinement XRD pattern of LNMO. **b)** Li/Ni disorder and Li slab thickness **c)** Lattice parameter. **d)** Refined Oxygen position in the lattice. **e)** Transition metal (TM) slab thickness of LNMO

The Li slab thickness and TM slab thickness were calculated from the equation below

Li slab thickness: 2*(1/3-oxygen position)*c lattice parameter

TM slab thickness: (c lattice parameter/3)-Li slab thickness[11]

Supporting Table 3. $LiNiO_2$ Rietveld refinement result

Rietveld refinement results of the $LiNiO_2$ sample using synchrotron powder XRD data

				$LiNiO_2$		
	space group			*R-3m*		
	a (Å), *c* (Å)			2.87608(1), 14.1983(1)		
atom	site		Wyckoff positions		occupancy[a]	*B* (Å^2)
Li1	3a	0	0	0	99.61	1[b]
Ni	3a	0	0	0	0.39	1[b]
Me[c]	3b	0	0	0.5	1.00	0.23(3)
O	6c	0	0	0.2403(2)	100[b]	0.14(7)
reliability factors				R_p = 10.5%, R_{wp} = 14.0%, R_{exp} = 8.31%, S = 1.68		

[a] The site occupation numbers in %
[b] Fixed parameter
[c] Transition metals (Ni)

Supporting Table 4. $LiNi_{0.90}Mn_{0.10}O_2$ Rietveld refinement result

Rietveld refinement results of the $LiNi_{0.90}Mn_{0.10}O_2$ sample using synchrotron powder XRD data

				$LiNi_{0.90}Mn_{0.10}O_2$		
	space group			*R-3m*		
	a (Å), *c* (Å)			2.87851(8), 14.2108(7)		
atom	site		Wyckoff positions		occupancy[a]	*B* (Å^2)
Li^+ 1	3a	0	0	0	96.8(3)	1[b]
Ni^{2+} 1	3a	0	0	0	3.2(3)	1[b]
Li^{1+} 2	3b	0	0	0.5	3.2(3)	0.28(4)
Ni^{2+} 2	3b	0	0	0.5	6.8(3)	0.28(4)
Ni^{3+}	3b	0	0	0.5	80[b]	0.28(4)
Mn^{4+}	3b	0	0	0.5	10[b]	0.28(4)
O	6c	0	0	0.2406(4)	100[b]	0.8(1)
reliability factors				R_p = 9.36%, R_{wp} = 12.0%, R_{exp} = 5.04%, S = 2.38		

[a] The site occupation numbers in %
[b] Fixed parameter

Supporting Table 5. $LiNi_{0.80}Mn_{0.20}O_2$ Rietveld refinement result

Rietveld refinement results of the $LiNi_{0.80}Mn_{0.20}O_2$ sample using synchrotron powder XRD data

				$LiNi_{0.80}Mn_{0.20}O_2$		
	space group			*R-3m*		
	a (Å), *c* (Å)			2.88051(2), 14.2387(2)		
atom	site		Wyckoff positions		occupancy[a]	*B* (Å^2)
Li^+ 1	3a	0	0	0	94.4(2)	1[b]
Ni^{2+} 1	3a	0	0	0	5.5(2)	1[b]
Li^{1+} 2	3b	0	0	0.5	5.5(2)	0.31(2)
Ni^{2+} 2	3b	0	0	0.5	14.4(2)	0.31(2)
Ni^{3+}	3b	0	0	0.5	60[b]	0.31(2)
Mn^{4+}	3b	0	0	0.5	20[b]	0.31(2)
O	6c	0	0	0.2411(1)	100[b]	0.78(6)
reliability factors				R_p = 6.63%, R_{wp} = 8.94%, R_{exp} = 5.33%, S = 1.67		

[a] The site occupation numbers in %
[b] Fixed parameter

Supporting Table 6. $LiNi_{0.70}Mn_{0.30}O_2$ Rietveld refinement result

Rietveld refinement results of the $LiNi_{0.70}Mn_{0.30}O_2$ sample using synchrotron powder XRD data

		$LiNi_{0.70}Mn_{0.30}O_2$				
space group		*R-3m*				
a (Å), *c* (Å)		2.88306(3), 14.2588(2)				
atom	site	Wyckoff positions			occupancy[a]	*B* (Å^2)
Li^+ 1	3a	0	0	0	92.8(2)	1[b]
Ni^{2+} 1	3a	0	0	0	7.1(2)	1[b]
Li^{1+} 2	3b	0	0	0.5	7.1(2)	0.28(1)
Ni^{2+} 2	3b	0	0	0.5	32.8(2)	0.28(1)
Ni^{3+}	3b	0	0	0.5	30[b]	0.28(1)
Mn^{4+}	3b	0	0	0.5	30[b]	0.28(1)
O	6c	0	0	0.2415(2)	100[b]	0.81(7)
reliability factors		R_p = 7.13%, R_{wp} = 9.59%, R_{exp} = 5.76%, S = 1.66				

[a] The site occupation numbers in %
[b] Fixed parameter

Supporting Table 7. $LiNi_{0.66}Mn_{0.34}O_2$ Rietveld refinement result

Rietveld refinement results of the $LiNi_{0.66}Mn_{0.34}O_2$ sample using synchrotron powder XRD data

				$LiNi_{0.66}Mn_{0.34}O_2$		
	space group			*R-3m*		
	a (Å), *c* (Å)			2.88487(3), 14.2702(2)		
atom	site		Wyckoff positions		occupancy[a]	*B* (Å^2)
Li^+ 1	3a	0	0	0	92.5(2)	1[b]
Ni^{2+} 1	3a	0	0	0	7.5(2)	1[b]
Li^{1+} 2	3b	0	0	0.5	7.5(2)	0.80(1)
Ni^{2+} 2	3b	0	0	0.5	26.5(2)	0.80(1)
Ni^{3+}	3b	0	0	0.5	32[b]	0.80(1)
Mn^{4+}	3b	0	0	0.5	34[b]	0.80(1)
O	6c	0	0	0.2416(2)	100[b]	1.33(6)
reliability factors				R_p = 9.48%, R_{wp} = 13.4%, R_{exp} = 10.2%, S = 1.31		

[a] The site occupation numbers in %
[b] Fixed parameter

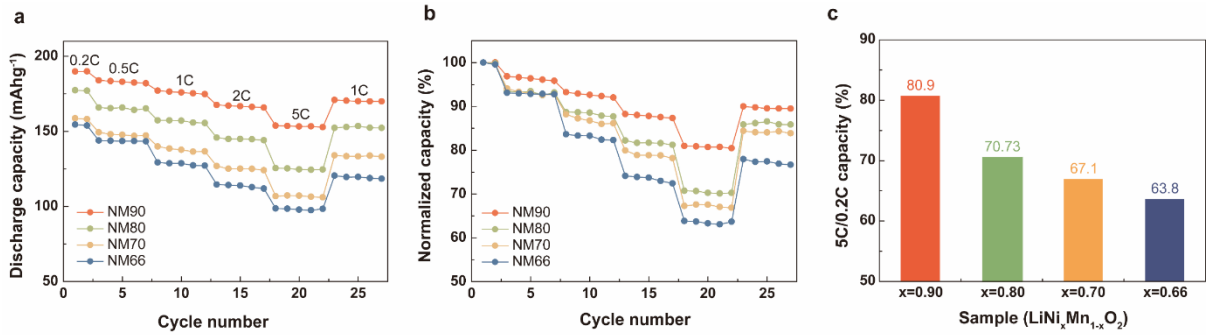

Figure S6. Rate capability of LNMO

a) Absolute discharge current density value of LNMO. **b)** 0.2C capacity normalized rate capability of LNMO. **c)** Capacity ratio of 5C charged capacity against 0.2C charged capacity

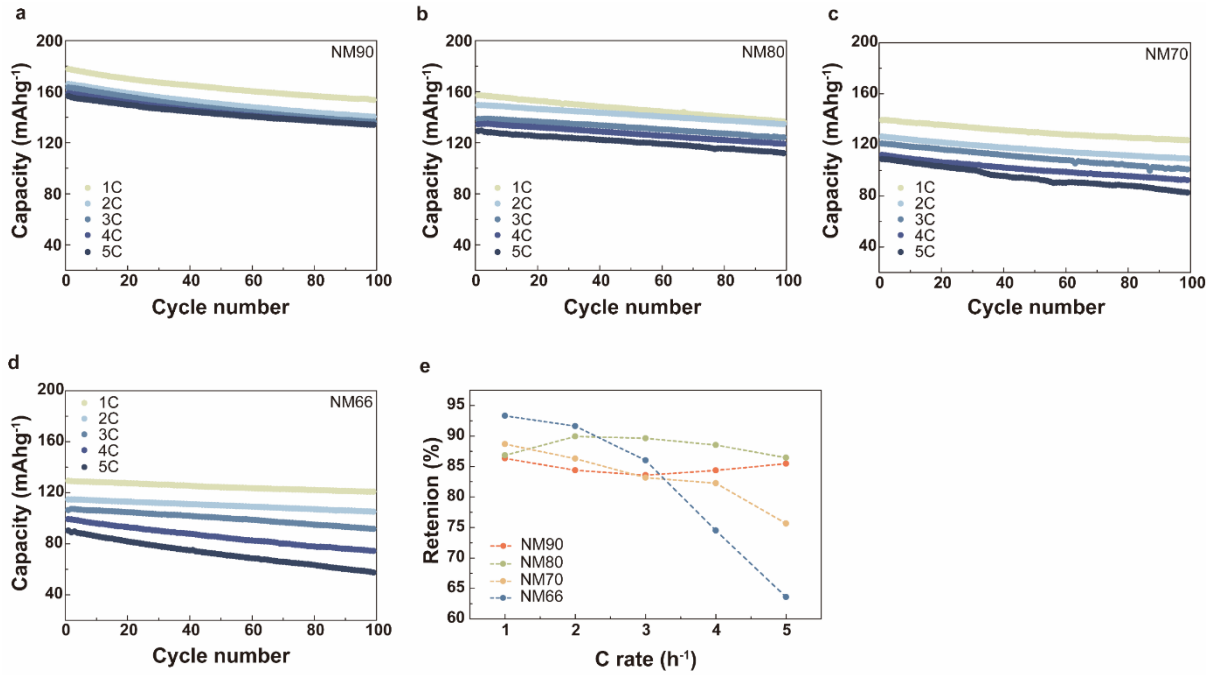

Figure S7. Cycle retention with different charging current rate of **a)** NM90. **b)** NM80. **c)** NM70. **d)** NM66. **e)** Cycle retention during 100 cycles at various charging rate

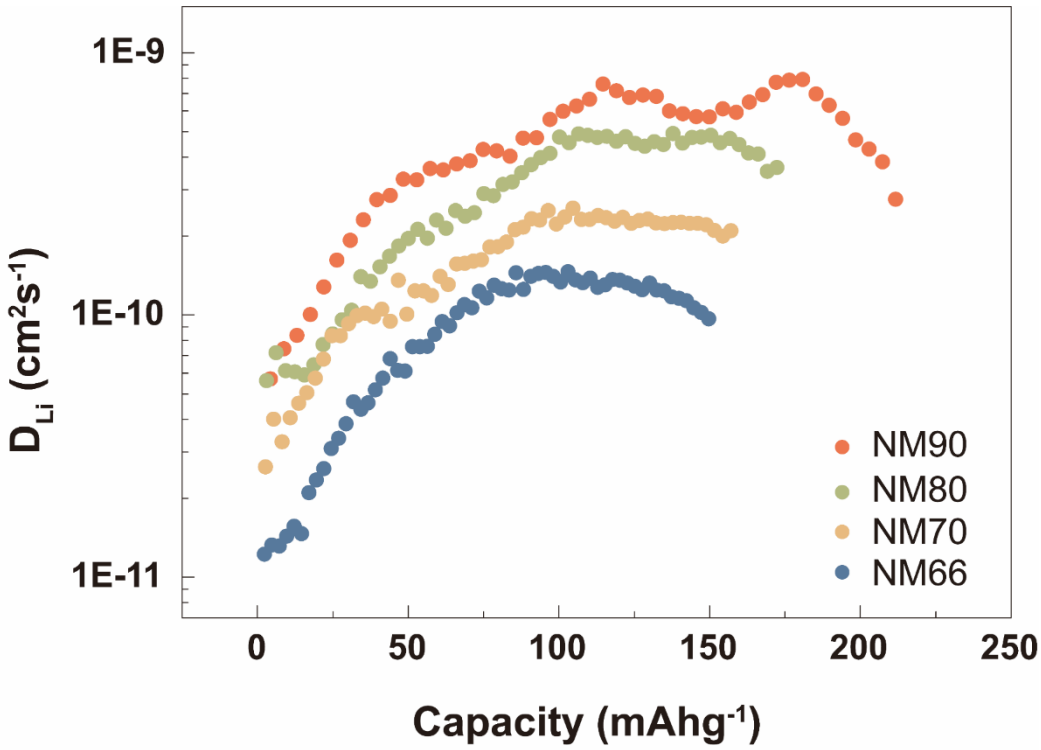

Figure S8. Li ion diffusivity of Co-free LNMO calculated from galvanostatic intermittent titration technique (GITT)

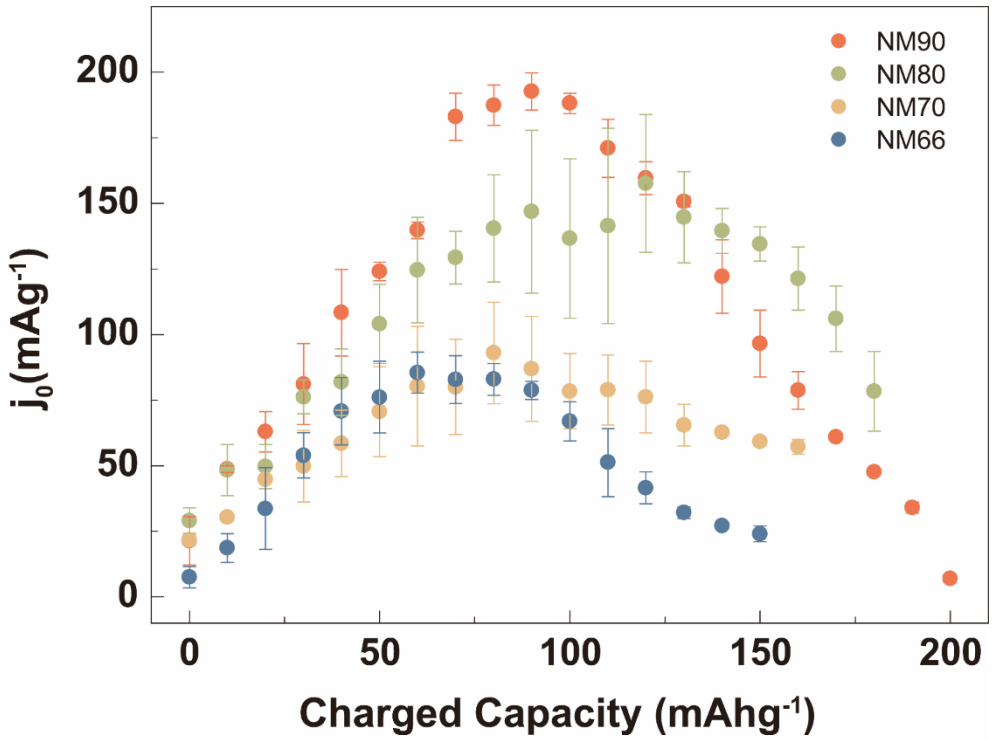

Figure S9. Exchange current density comparison of NM90 and NM66 calculated from electrochemical impedance spectroscopy (EIS) with equation $j_0 = \frac{RT}{F}\frac{1}{R_{interface}}$.

The data were collected in two coin cells

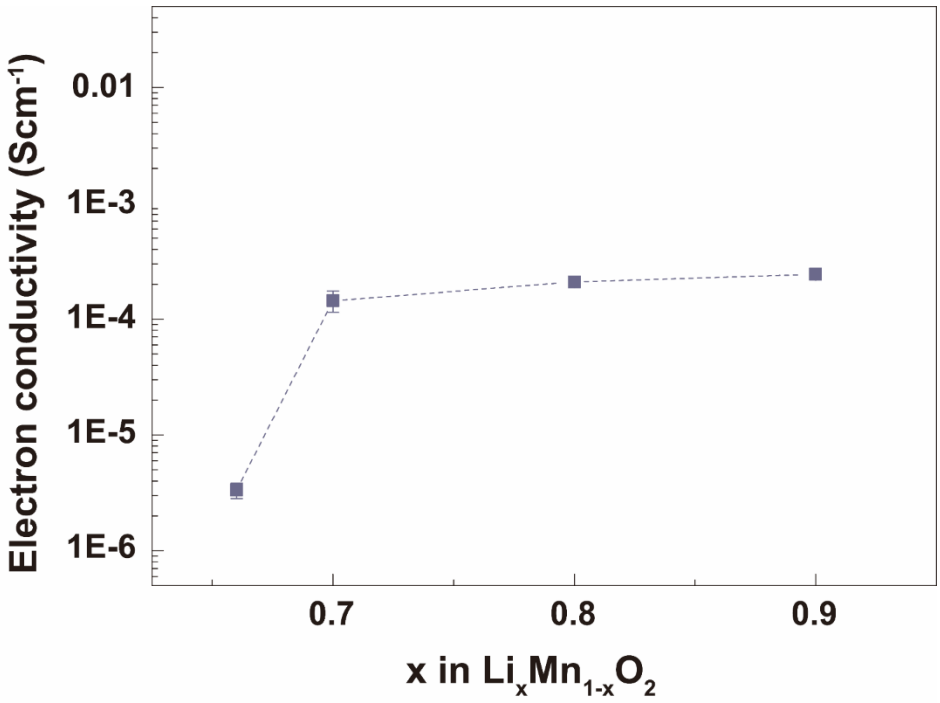

Figure S10. Electron conductivity of Co-free LNMO

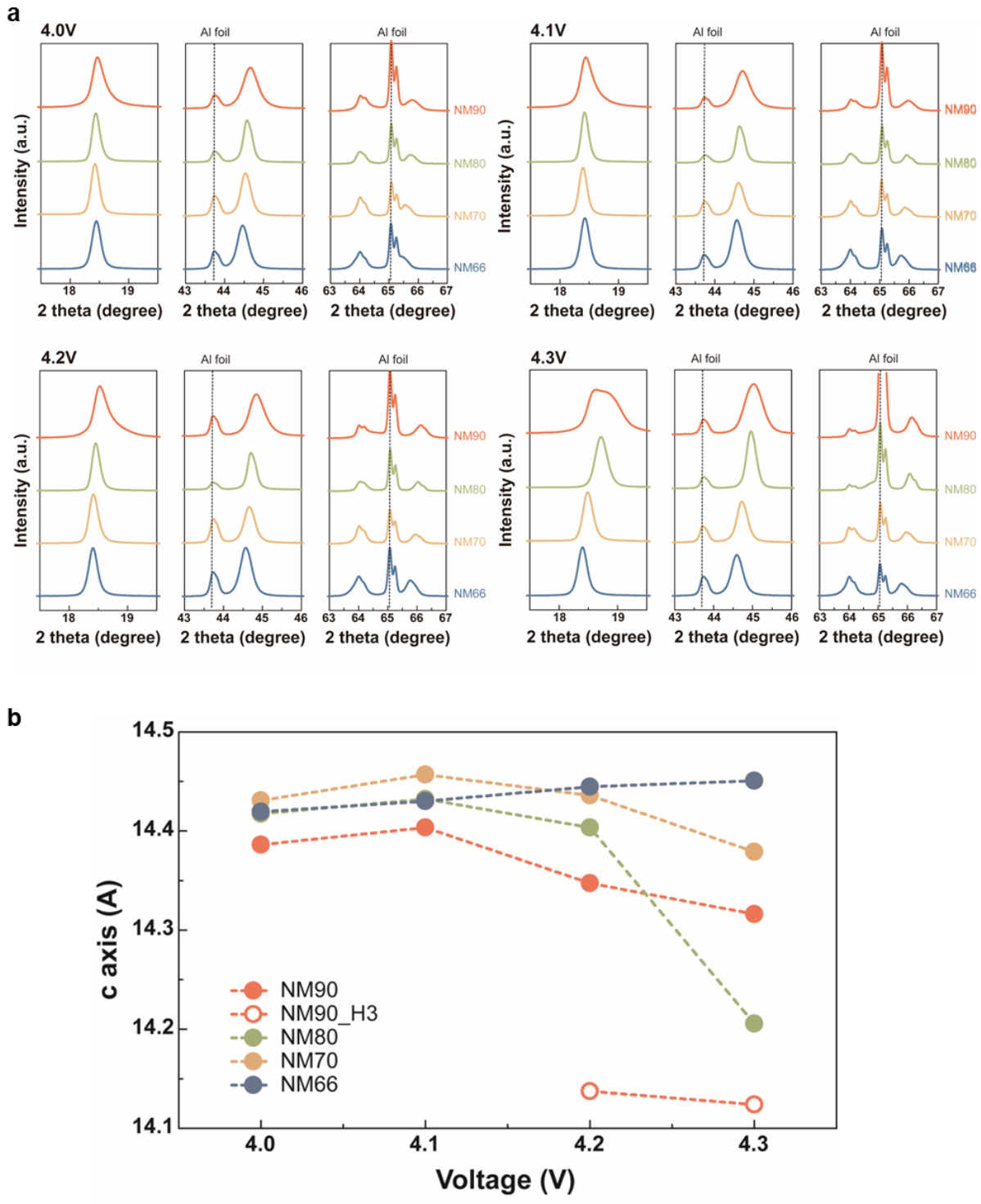

Figure S11. a) Ex-situ XRD plot at different cut-off voltage b) Calculated c-axis parameter from (003) peak position. Δc_{max} of NM90, NM80, NM70 and NM66 are -1.98%, -1.59%, -0.54% and 0.14% respectively.

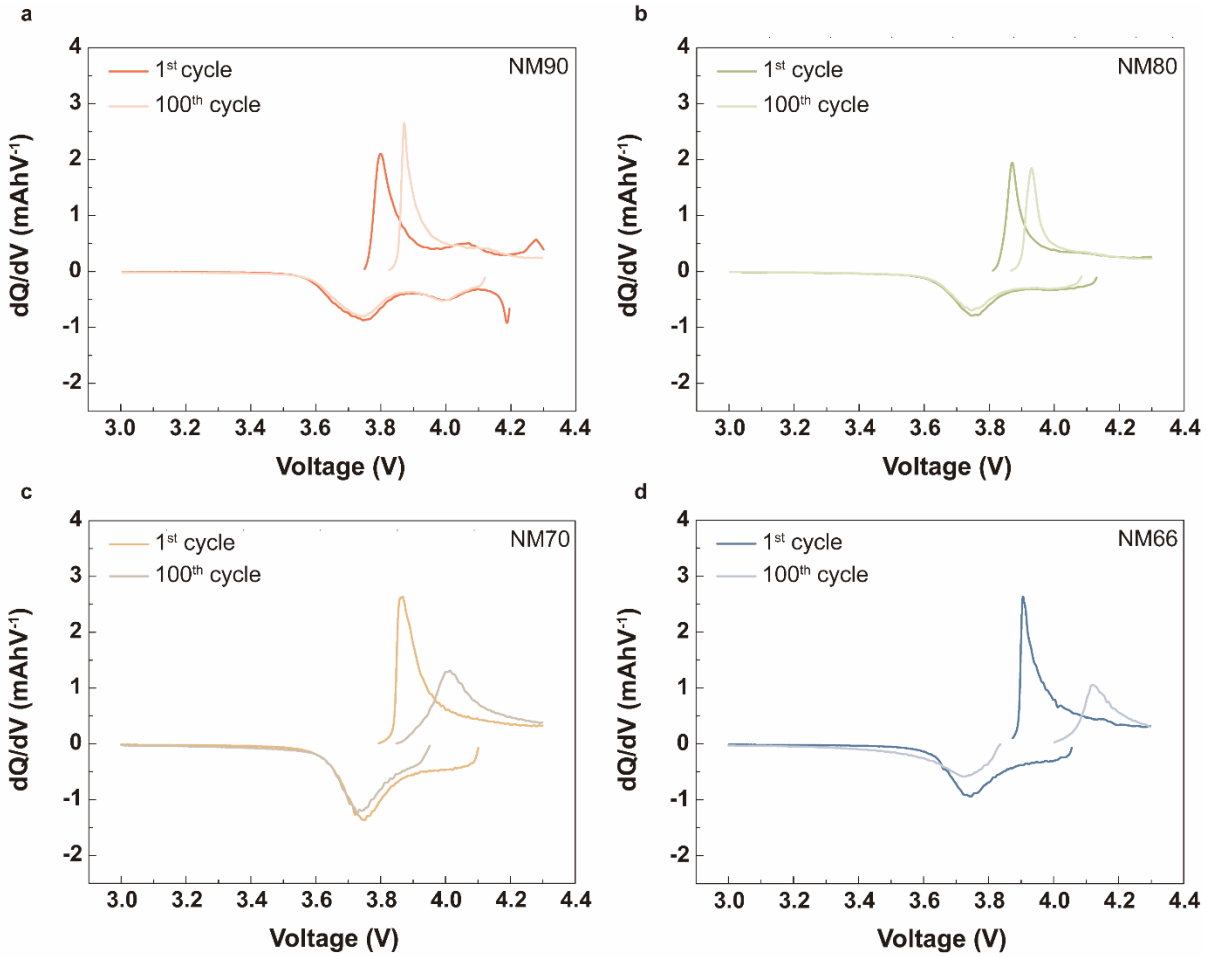

Figure S12. Cycle reversibility after extreme fast charging cycle of **a)** NM90. **b)** NM80. **c)** NM70. **d)** NM66.

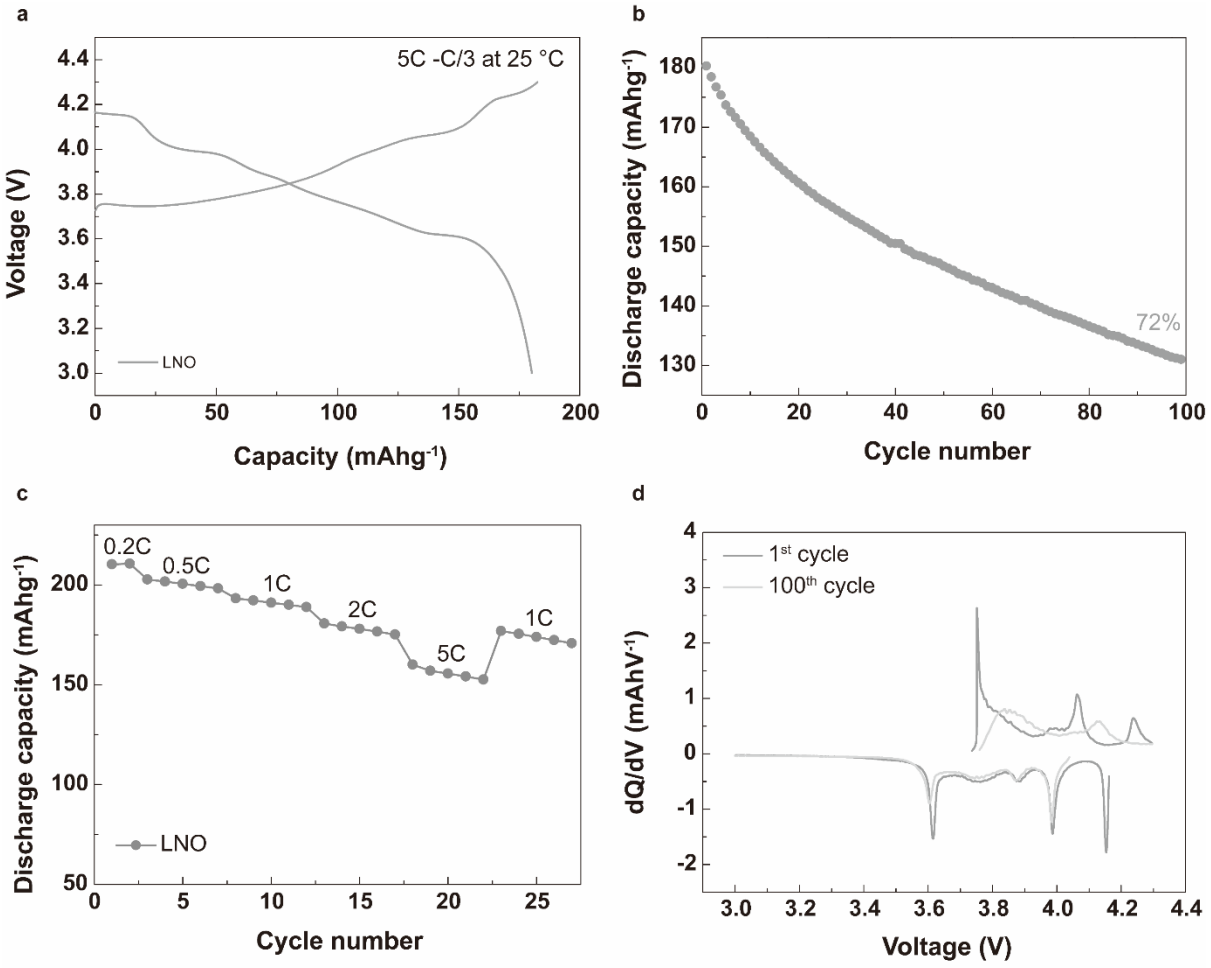

Figure S13. Electrochemical analysis of LNO **a)** Galvanostatic profile of first cycle with XFC cycling. **b)** Cycle retention of 100 cycles. **c)** dQ/dV after 100 cycles and **d)** Rate capability of LNO

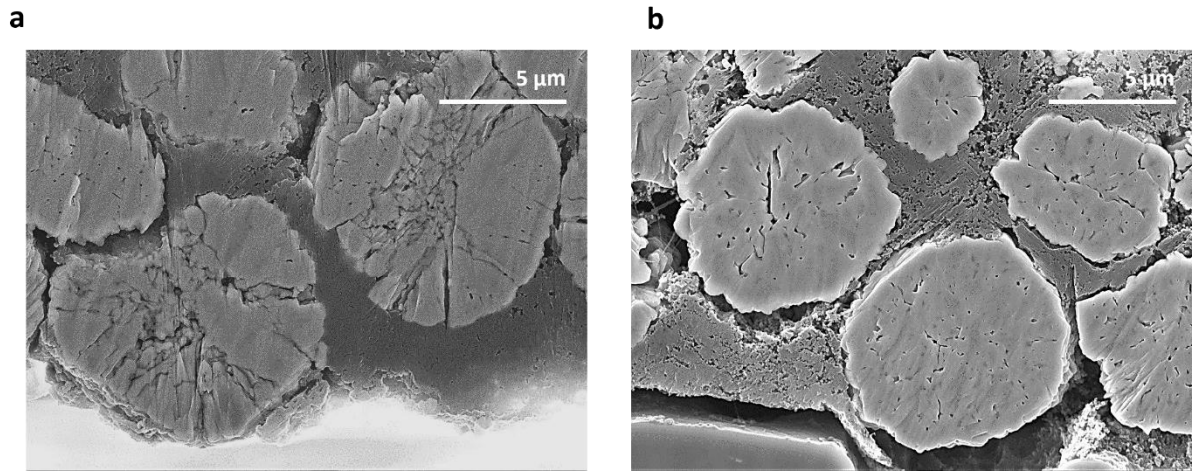

Figure S14. SEM image after 1C & -C/3 cycle of **a)** NM90 and **b)** NM66.

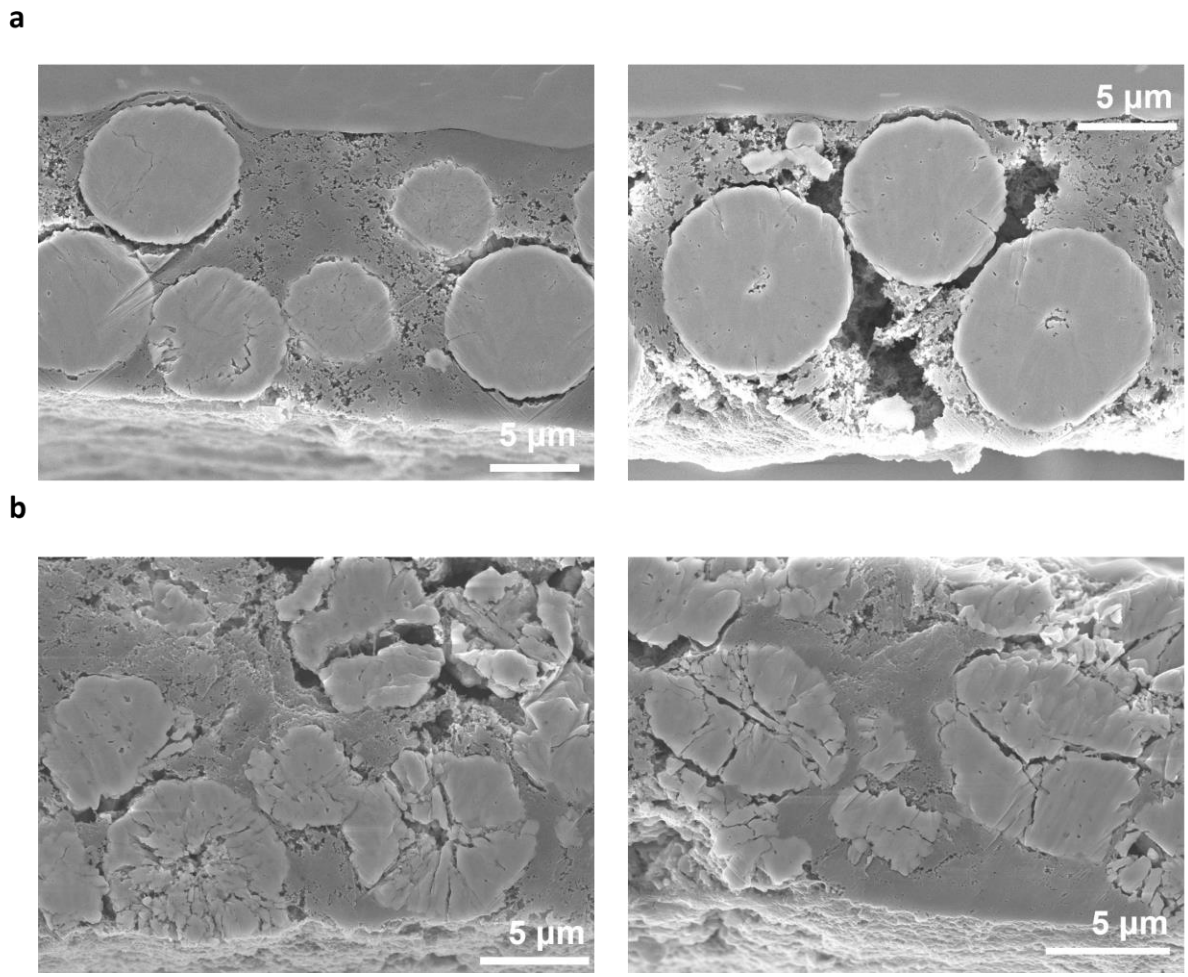

Figure S15. SEM image after 5C & -C/3 cycle of **a)** NM90 and **b)** NM66.

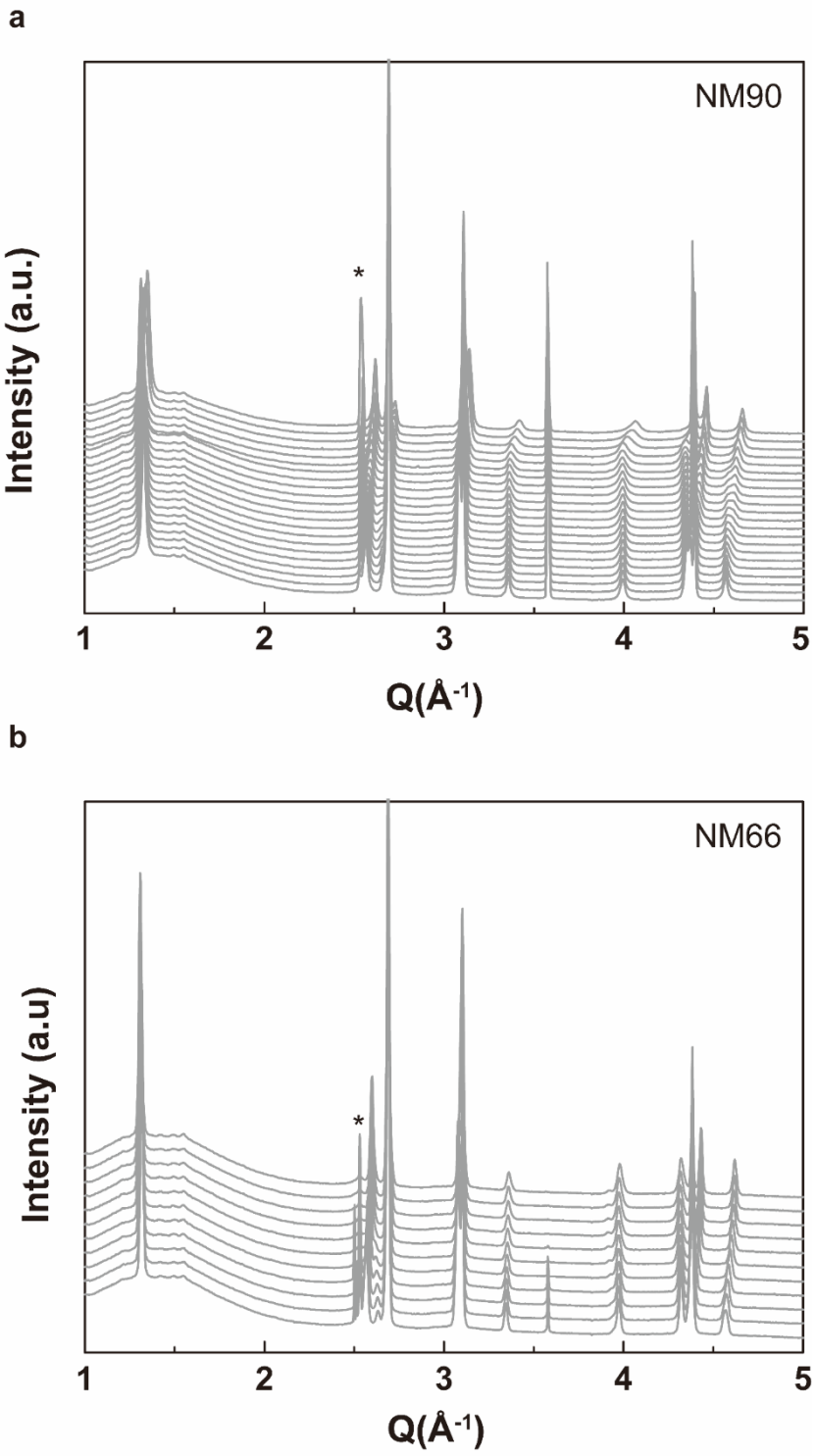

Figure S16. In-situ XRD of 0.1C charged **a)** NM90 and **b)** NM66

The * indicates the beam saturated data not the impurity or peak separation

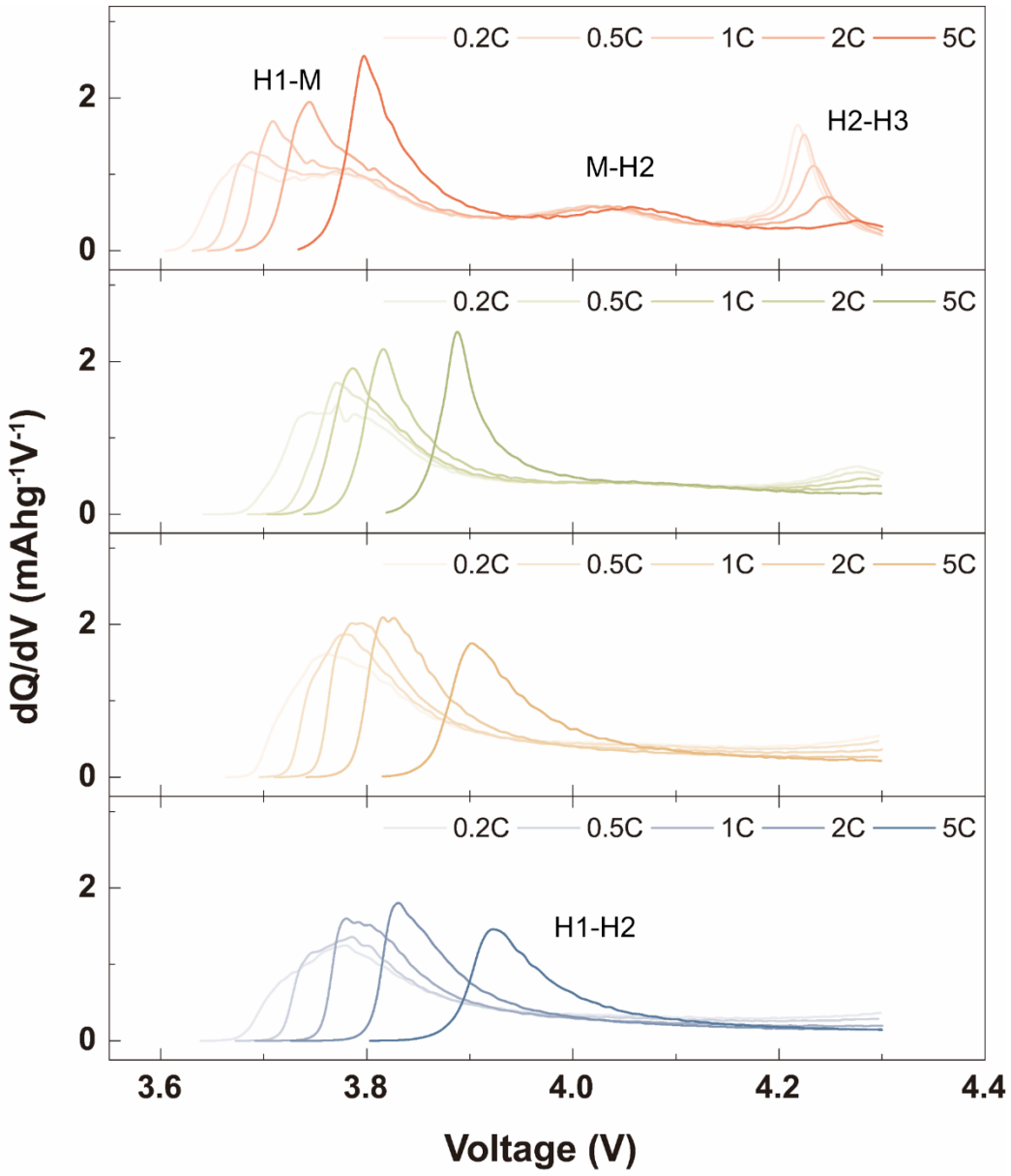

Figure S17. Charging current dependent phase transition of Co-free LNMO

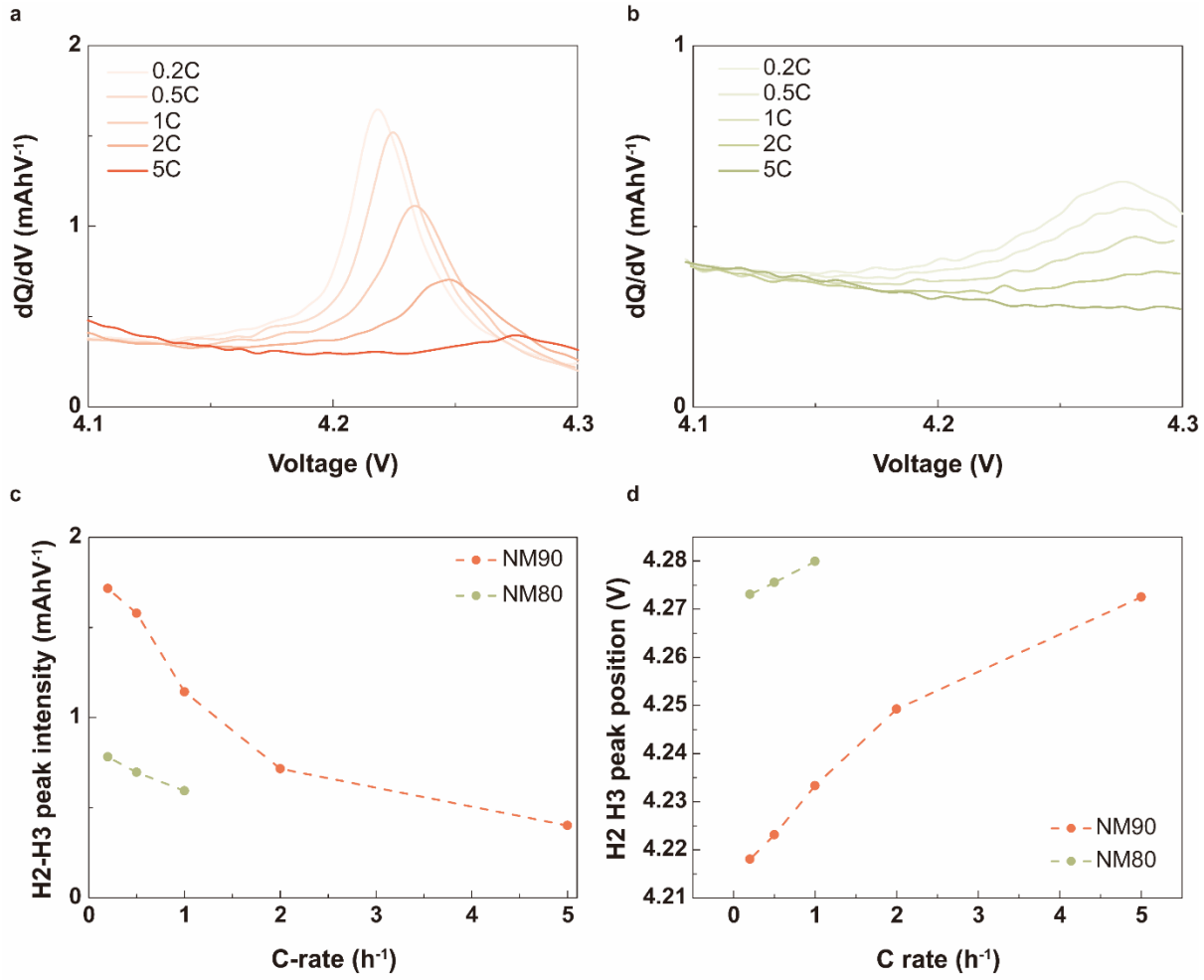

Figure S18. Enlarged dQ/dV profile of Ni rich LNMO of **a)** NM90 and **b)** NM80. The correlation of charging current density with **c)** H2-H3 peak intensity, and **d)** H2-H3 peak position.

The decrease of the peak intensity indicate that the H2-H3 transition were suppressed at higher charging current rate and the peak position shift of H2-H3 transition suggests that the suppression was occur from kinetic factor.

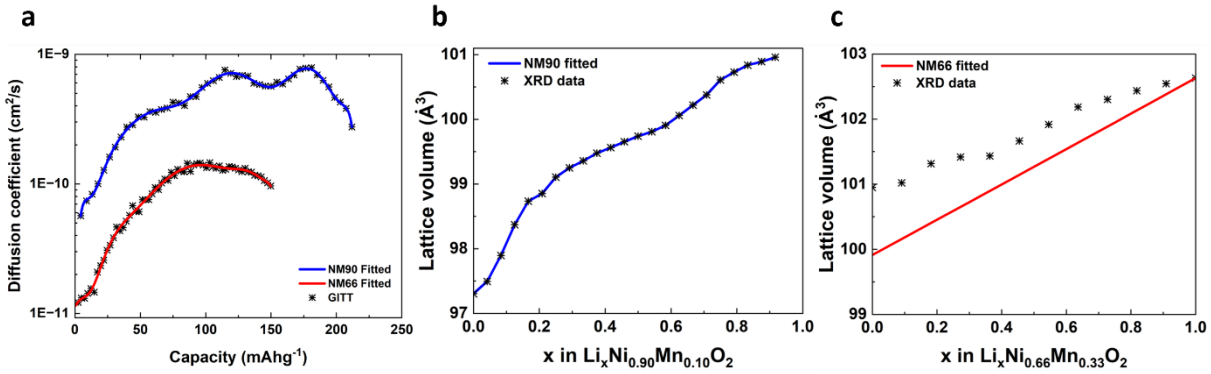

Figure S19. SOC dependent parameters for finite element analysis **a)** Li ion diffusivity coefficient from GITT analysis and fitted value **b)** Lattice volume evolution of NM90 with H2-H3 phase transition **c)** Lattice volume of NM66 without abrupt lattice change

Supporting Table S8. Simulated parameters of diffusion-induced stress and fracture simulation of NM particles[6, 12]

Symbol	Value	Description	Ref.
E_{NM90}	135 GPa	Elastic modulus of NM90	
E_{NM66}		Elastic modulus of NM66	
ν_{NM90}	0.3	Poisson's ratio of NM90	
ν_{NM66}		Poisson's ratio of NM66	
$c_{max,NM90}$	49777.22 mol/m^3	Stoichiometric Li concentration of NM90	
$c_{max,NM66}$	49315.93 mol/m^3	Stoichiometric Li concentration of NM66	
r	3.5 μm	Radius of NM particles	
G_c	0.11 J/m^2	Critical energy release rate of NM particles	[6]
σ_t	10 MPa	Tensile strength	[6]
K	5×10^{15} N/m^3	Penalty factor	[12]

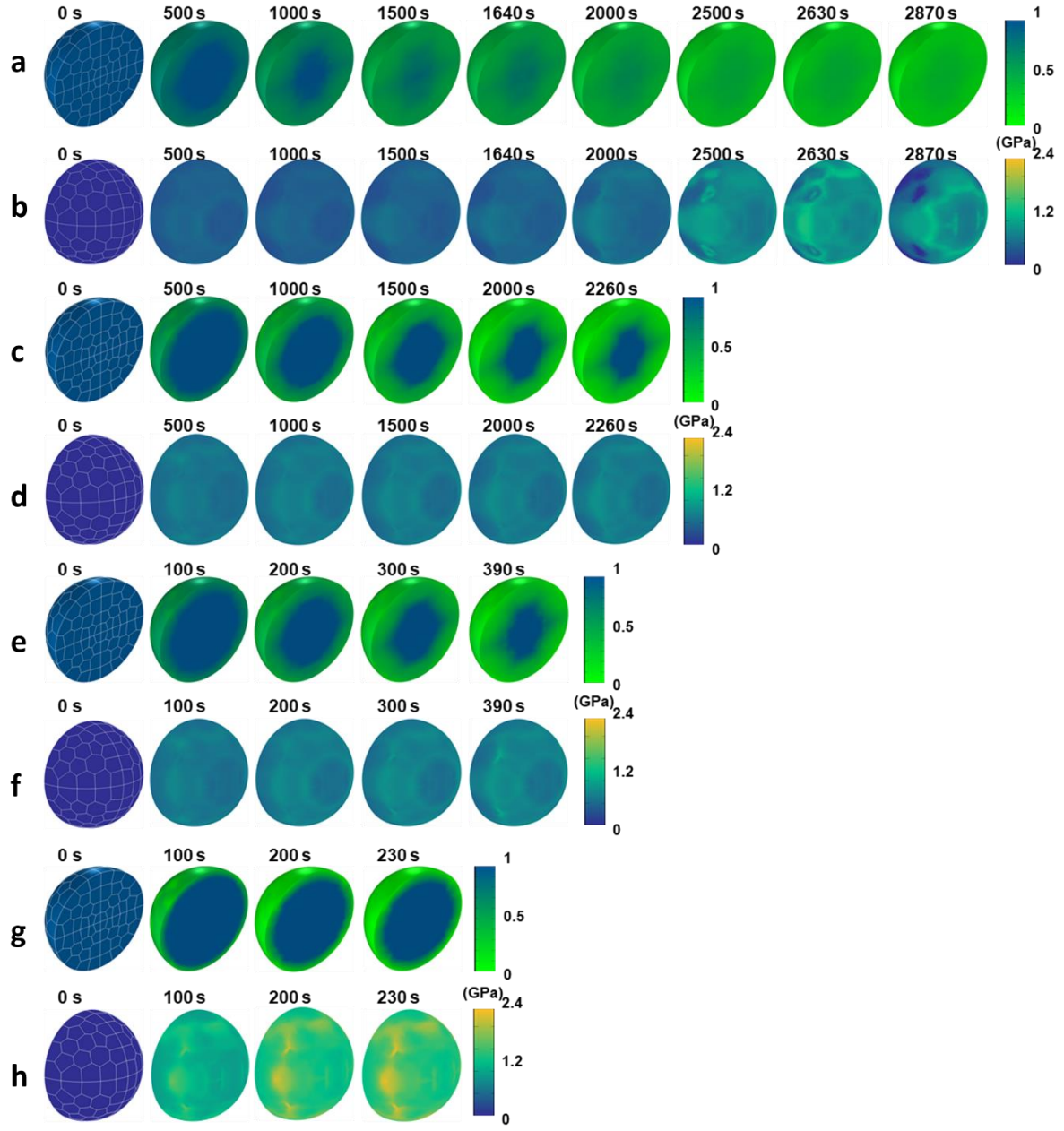

Figure S20. Concentration and first principal stress contour of entire geometry during charging process of **a), b)** NM90 with 1C, **c), d)** NM66 with 1C, **e), f)** NM90 with 5C, **g), h)** NM66 with 5C.

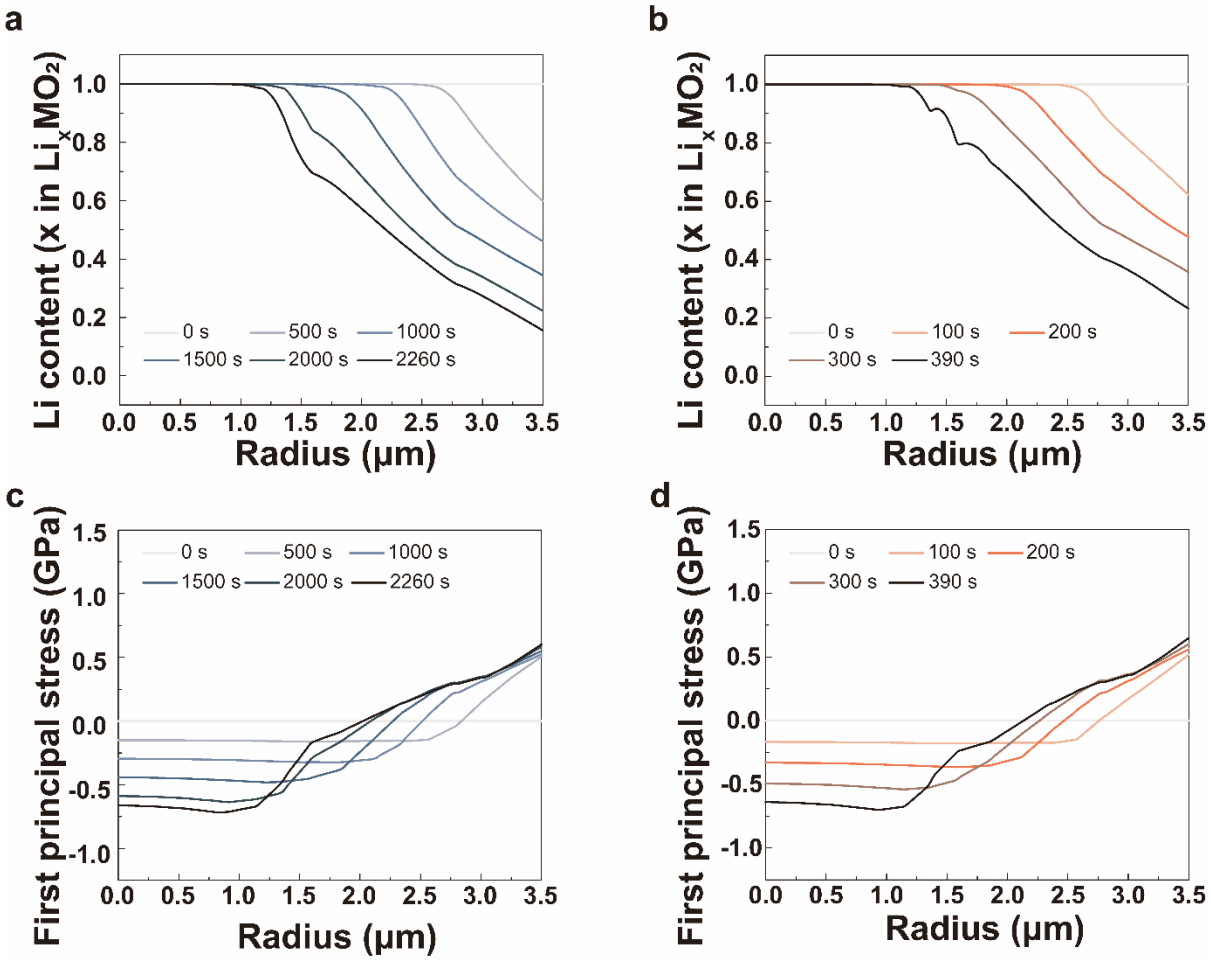

Figure S21. Intra secondary particle SOC heterogeneity and stress under different cycling condition

Li ion concentration of a) 1C charged NM66 and b) 5C charged NM90. First principal stress of c) 1C charged NM66 and d) 5C charged NM90

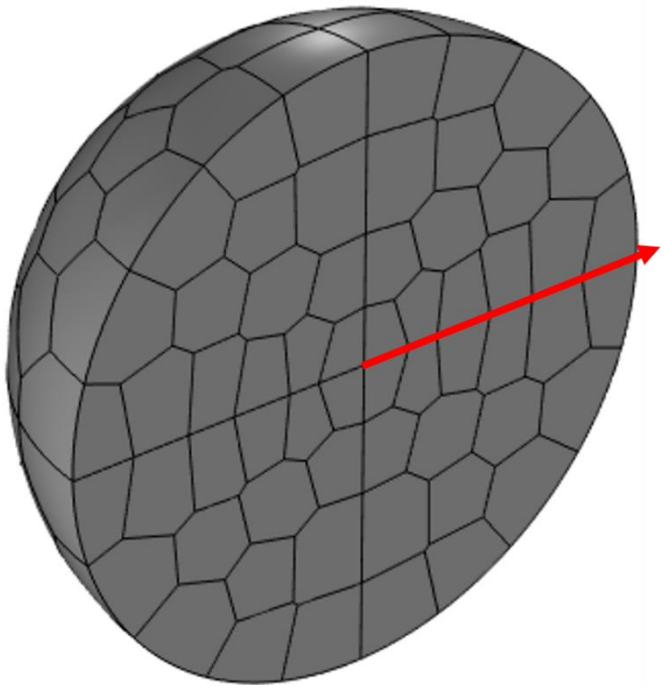

Figure S22. Reference axis for concentration and stress generation profile

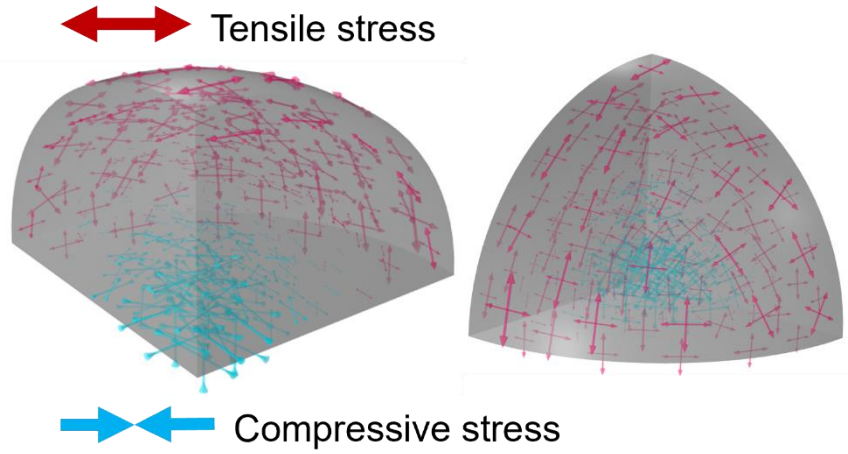

Figure S23. Stress evolution during electrochemical delithiation of Co-free LNMO

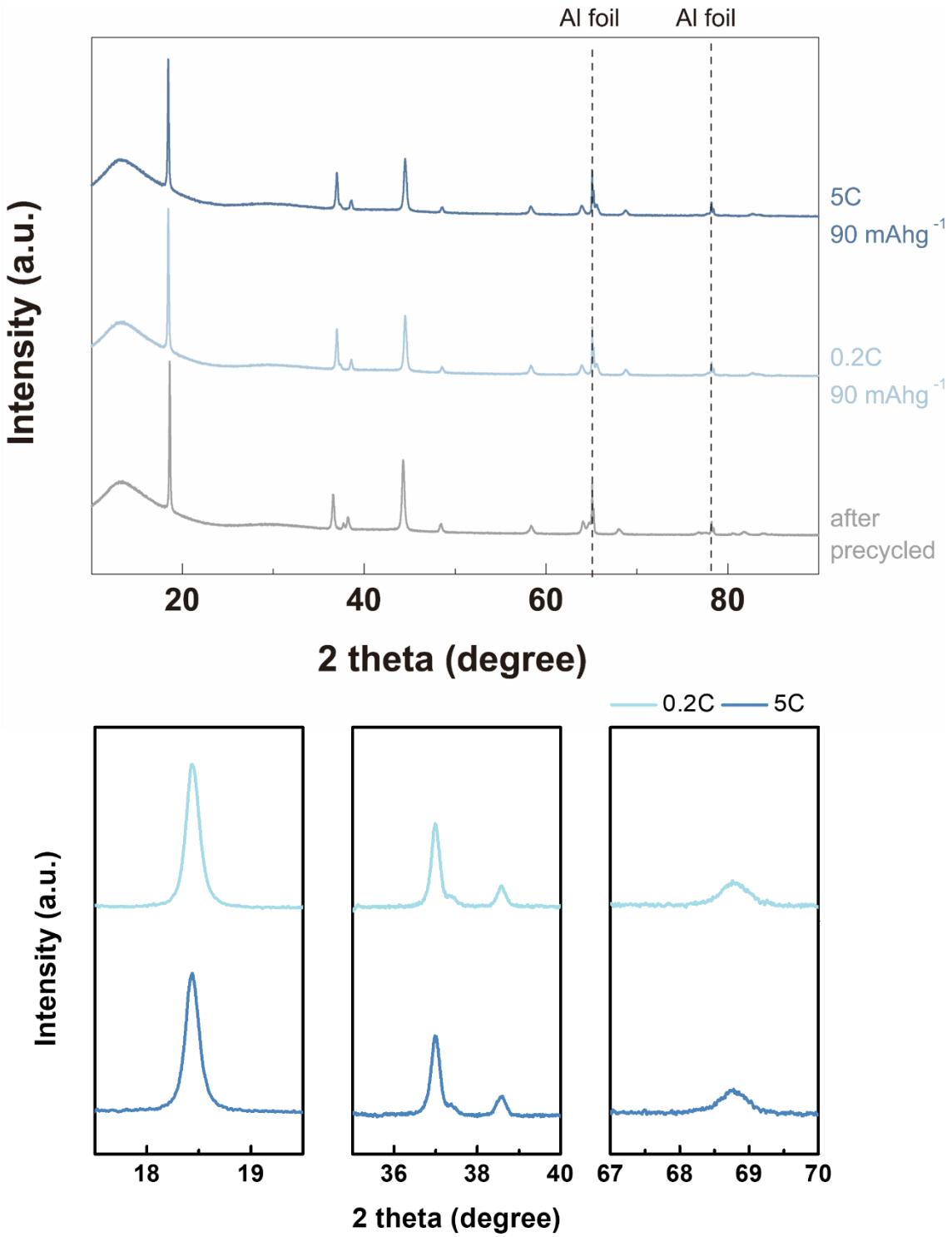

Figure S24. Quenched XRD of NM66 after electrochemical cycling. The zero-shift error were aligned using electrochemically inactive Al foil. The XRD measurement were conducted using Cu Kα source.

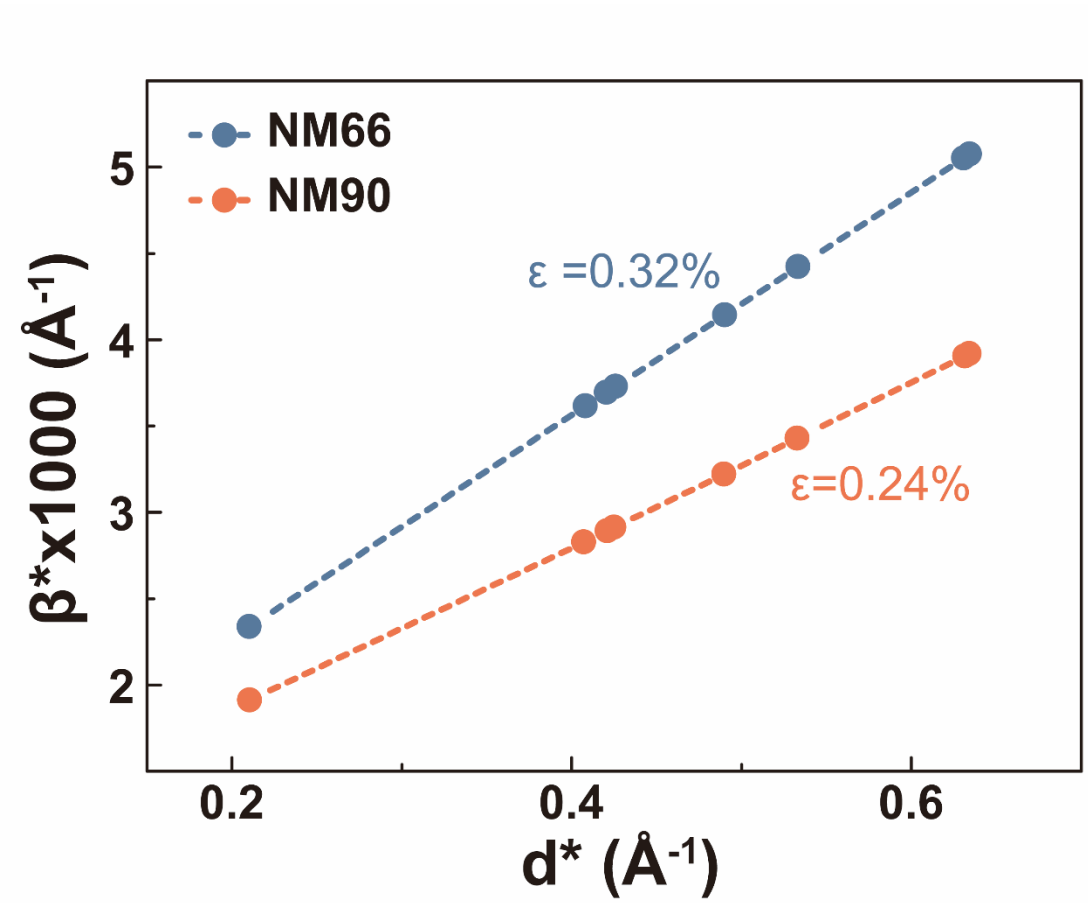

Figure S25. Williamson-Hall plot of 5C charged and quenched NM66 and NM90.

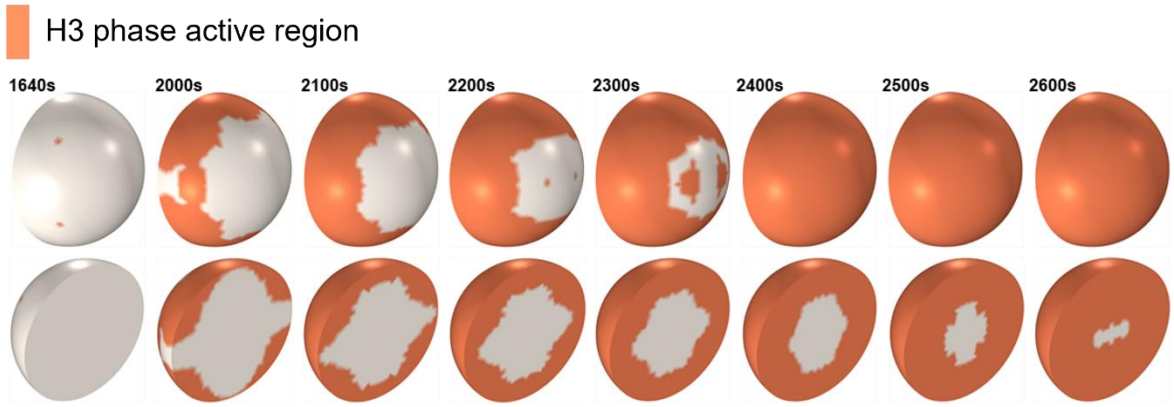

Figure S26 a) H2-H3 transition propagation of NM90, orange marked region is H3 phase

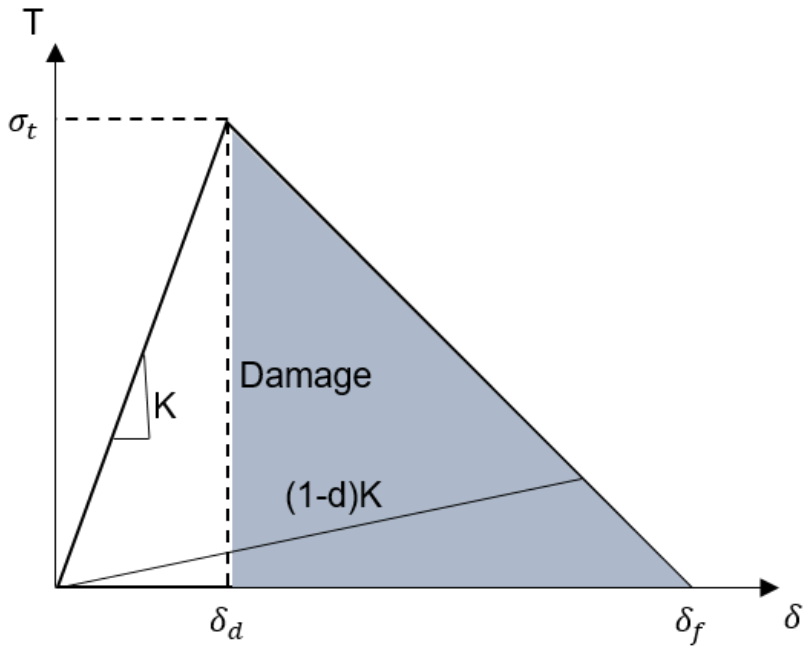

Figure S27. Bilinear traction-separation relationship for cohesive zone model

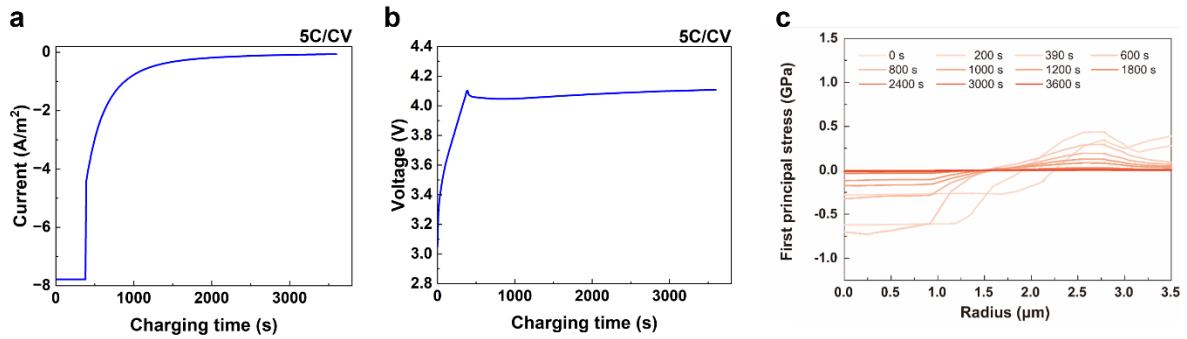

Figure S28. Simulation results of 5C/CV charged NM90.

a) Charging current **b)** Voltage profile and **c)** stress evolution during 5C/CV charging

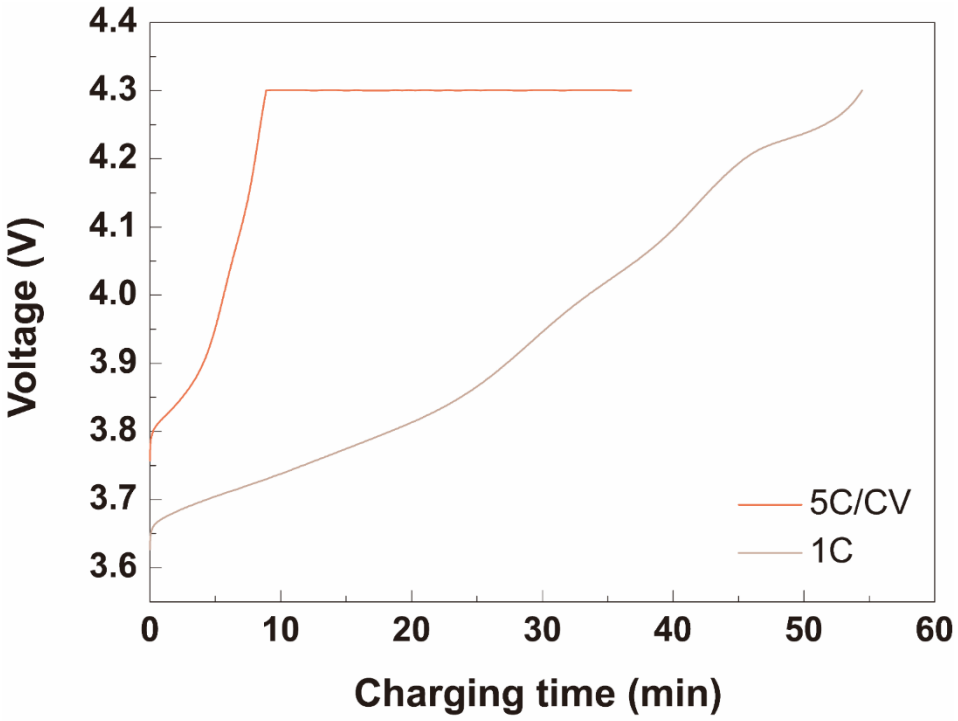

Figure S29. Charging time of different charging protocol

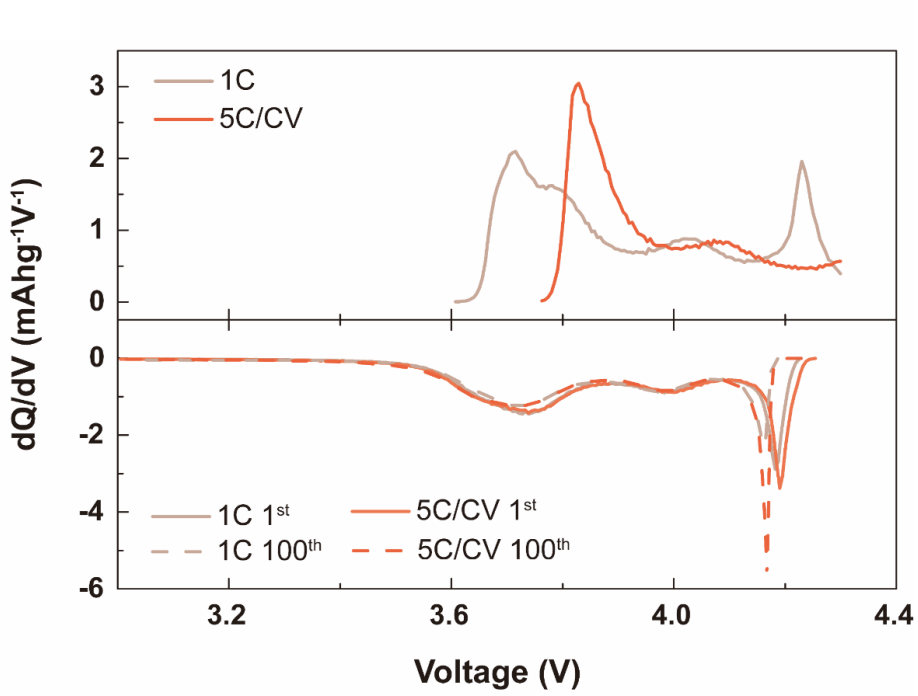

Figure S30. dQ/dV data of NM90 with different charging protocol

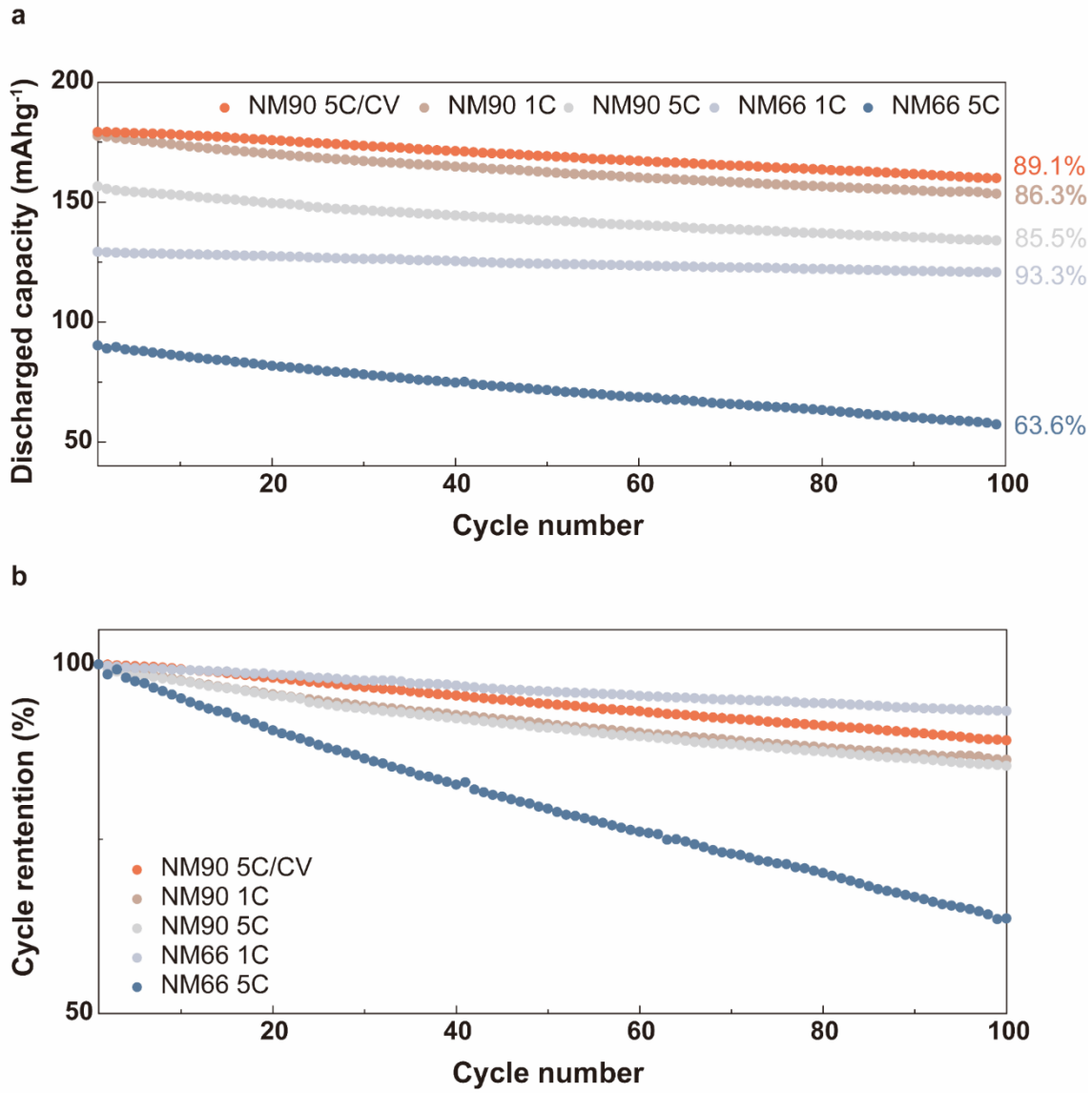

Figure S31. a) Discharge capacity and **b)** cycle retention of Co-free LNMO under various cycling condition.

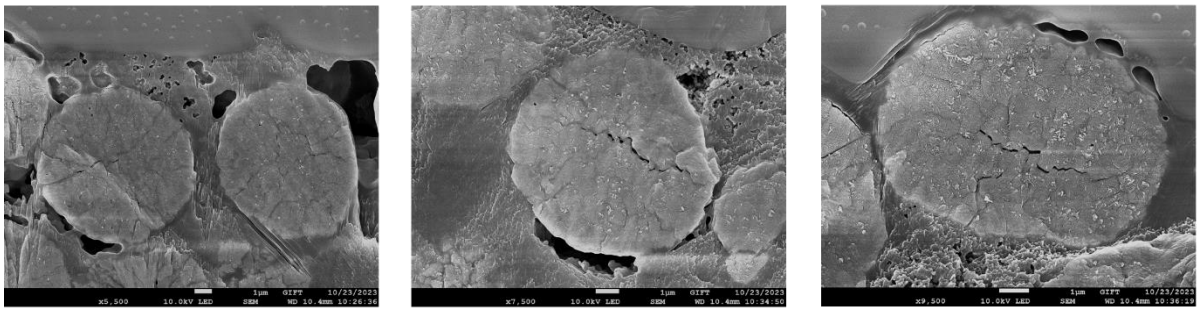

Figure S32. Cross section SEM of 5C/CV charged NM90

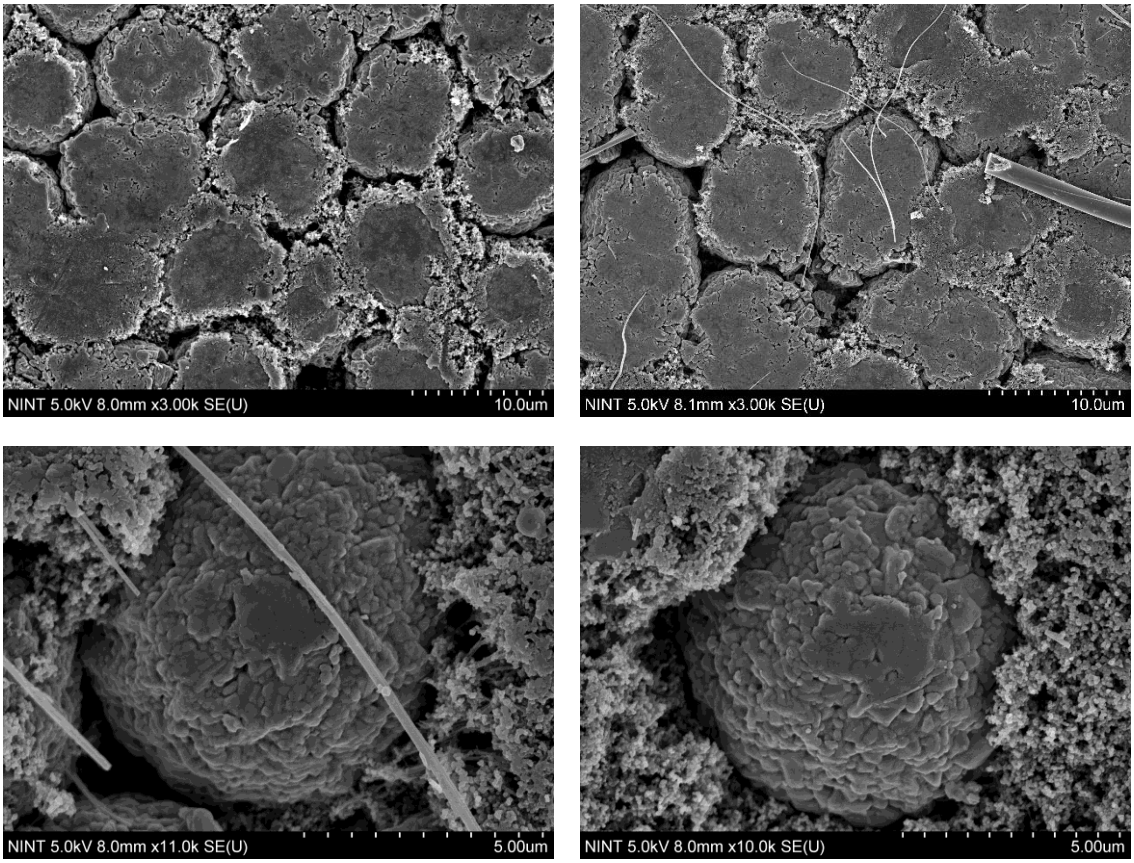

Figure S33. Top- view SEM of 5C/CV charged NM90. The fibers are from GF/F separator.

Supporting Table S9. Efficiency of 5C/CV charging for fast chargeable cathode[13-18]

Cathode	Charging protocol (Voltage window)	Capacity ($mAhg^{-1}$)	Cycle retention (%)	Material Modification	Ref
NM90	**5C/CV (3.0 V - 4.3 V)**	**180**	**89.1 @ 100cyc**	**No**	**This work**
Ns-NM90	3C (2.7 V - 4.4 V)	~210	85.2 @ 100 cyc	Core-shell design & Microstructure	[13]
NM90	3C (2.7 V - 4.4 V)	~205	76.1 @ 100 cyc	No	[13]
Ta-NCM90	2C (2.7 V – 4.3 V)	~212.3	94.7 @ 100 cyc	Doping & Microstructure	[14]
NCM90	2C (2.7 V – 4.3 V)	~207.2	86.8 @ 100 cyc	No	[14]
EEC-Ni90	5C (2.5 V – 4.3 V)	~150	84.38 @ 200 cyc	High entropy coating	[15]
NCM811	3C (2.8 V – 4.3 V)	161.4	76.78 @ 200 cyc	No	[16]
NCM83	1C/CV (2.0 V – 4.3 V)	195.3	58.3 @ 200 cyc	No	[17]
Al doped NM90	5C (2.7 V – 4.3 V)	158.3	86.4 @ 100 cyc	Doping	[18]

1. J. Moon, J. Y. Jung, T. D. Hoang, D. Y. Rhee, H. B. Lee, M.-S. Park and J.-S. Yu, *Journal of Power Sources*, 2021, **486**, 229359.
2. S. Lou, Q. Liu, F. Zhang, Q. Liu, Z. Yu, T. Mu, Y. Zhao, J. Borovilas, Y. Chen and M. Ge, *Nature Communications*, 2020, **11**, 5700.
3. X. Zhang, W. Shyy and A. M. Sastry, *Journal of the Electrochemical Society*, 2007, **154**, A910.
4. S. C. Cowin, *Mechanics of materials*, 1985, **4**, 137-147.
5. Y. Gwak, J. Moon and M. Cho, *Journal of Power Sources*, 2016, **307**, 856-865.
6. R. Xu, L. De Vasconcelos, J. Shi, J. Li and K. Zhao, *Experimental mechanics*, 2018, **58**, 549-559.
7. G. Sun, X. Yin, W. Yang, A. Song, C. Jia, W. Yang, Q. Du, Z. Ma and G. Shao, *Physical Chemistry Chemical Physics*, 2017, **19**, 29886-29894.
8. K. Chen, P. Barai, O. Kahvecioglu, L. Wu, K. Z. Pupek, M. Ge, L. Ma, S. N. Ehrlich, H. Zhong and Y. Zhu, *Nature Communications*, 2024, **15**, 430.
9. H. Park, H. Park, K. Song, S. H. Song, S. Kang, K.-H. Ko, D. Eum, Y. Jeon, J. Kim and W. M. Seong, *Nature Chemistry*, 2022, **14**, 614-622.
10. T. Liu, L. Yu, J. Liu, J. Lu, X. Bi, A. Dai, M. Li, M. Li, Z. Hu and L. Ma, *Nature Energy*, 2021, **6**, 277-286.
11. W. Lee, S. Muhammad, T. Kim, H. Kim, E. Lee, M. Jeong, S. Son, J. H. Ryou and W. S. Yoon, *Advanced Energy Materials*, 2018, **8**, 1701788.
12. S. Rezaei, A. Asheri and B.-X. Xu, *Journal of the Mechanics and Physics of Solids*, 2021, **157**, 104612.
13. G. T. Park, H. H. Sun, T. C. Noh, F. Maglia, S. J. Kim, P. Lamp and Y. K. Sun, *Advanced Energy Materials*, 2022, **12**, 2202719.
14. N. Y. Park, M. C. Kim, S. M. Han, G. T. Park, D. H. Kim, M. S. Kim and Y. K. Sun, *Angewandte Chemie International Edition*, 2024, **63**, e202319707.
15. C. Zhao, C. Wang, X. Liu, I. Hwang, T. Li, X. Zhou, J. Diao, J. Deng, Y. Qin and Z. Yang, *Nature Energy*, 2024, **9**, 345-356.
16. S. Ma, X. Zhang, S. Wu, E. Fan, J. Lin, R. Chen, F. Wu and L. Li, *Energy Storage Materials*, 2023, **55**, 556-565.
17. J. Y. Park, M. Jo, S. Hong, S. Park, J. H. Park, Y. I. Kim, S. O. Kim, K. Y. Chung, D. Byun and S. M. Kim, *Advanced Energy Materials*, 2022, **12**, 2201151.
18. H. Feng, Y. Leng, T. Chen, Y. Sun, C. Hai and Y. Zhou, *Journal of Alloys and Compounds*, 2023, **960**, 170676.